Conduit processes during the February 11, 2010 Vulcanian eruption of Soufrière Hills, Montserrat

Alain BURGISSER[1*], Tonin BECHON[2], Laure CHEVALIER[1,3], Marielle COLLOMBET[1], Laurent ARBARET[4], Mélanie FORIEN[5]

[1] Univ. Grenoble Alpes, Univ. Savoie Mont Blanc, CNRS, IRD, IFSTTAR, ISTerre, 38000 Grenoble, France.

[2] Département de Géologie, Université de Liège, Allée du Six Août 12, 4000 Sart Tilman, Belgium.

[3] Now at: Institut für Geowissenschaften, Goethe Universität, Altenhöferallee 1, 60348 Frankfurt am Main, Germany.

[4] Institut des Sciences de la Terre d'Orléans (ISTO), Université d'Orléans-CNRS-BRGM, Orléans, France.

[5] Department of Geosciences, UiT The Arctic University of Norway in Tromsø, 9037 Tromsø, Norway.

Abstract: 250 words, Main text: 8400 words, 3 Tables, 7 Figures, 88 references.

* Corresponding author: Phone: (+33) 479 758 780. Fax: (+33) 479 758 742. Email: alain.burgisser@univ-savoie.fr

Abstract

We analyzed pumice from the February 11, 2010 Vulcanian explosion that immediately followed a large dome collapse at Soufrière Hills volcano. We obtained pre-explosive values of porosity, pressure, and depth by combining textural analyses and glass water content determinations. Our data suggest that the February 2010 explosion evacuated the upper 3 km of the conduit from the dense magma (≤10 vol.% porosity) it contained. The low porosity distribution in the volcanic conduit implies that the magma rising from the reservoir had time to extensively degas during emplacement. We use a conduit flow model to characterize the effects of permeability on ascent conditions. Model input parameters were fitted so as to match our pre-explosive porosity data, which yielded first-order constraints on conduit radius, mass flux, outgassing efficiency, and permeability. This parametric study suggests that efficient lateral gas escape is necessary to explain the low pre-explosive porosities. Steady-state solutions fitting the observed range of dome extrusion rate in the month preceding the February 11 event suggest permeabilities $<10^{-13}$ m^2 deeper than 500 m, which are values typical of crack-supported permeability. Conversely, solutions with parameters consistent with bubble-supported permeability imply transient flow conditions prior to the February 11 event. The transient conditions imply that our data represent a snapshot of the porosity distribution within the conduit that does not preclude the temporary presence of much higher porosities in the conduit. Such unsteady conduit flow conditions are consistent with the irregular but active dome growth in the month prior to the February 11 event.

Keywords: fluid dynamics; magma porosity; magma permeability; textural analysis

1. Introduction

Vulcanian explosions are short-lived but powerful events that evacuate parts of the magma present in a volcanic conduit. They often take place during dome eruptions, with little to no precursor signs (Clarke et al., 2015). Their occurrence and intensity is closely linked to magma decompression, degassing, and outgassing (Spieler et al., 2004; Mueller et al., 2011). The current eruption at Soufrière Hills volcano, Montserrat, is an ideal case to shed light on what conditions the occurrence of Vulcanian explosions. Soufrière Hills has produced over the last two decades a remarkable range of such events, from explosions series separated by a few hours to isolated explosions of variable intensity (Druitt and Kokelaar, 2002; Wadge et al., 2014a). Some explosions were closely following partial dome collapse, whereas others occurred in the absence of dome. Previous studies of pre-explosive conduit conditions at Soufrière Hills volcano were done by Clarke et al. (2007), Burgisser et al. (2010), and Burgisser et al. (2011). They have shown that the magma filling the conduit prior to Vulcanian explosions consisted of a dense cap atop the conduit with a thickness of a few tens of meters, a 200–700 m thick region with heterogeneous vesicularities, and, at greater depth, a more homogeneous, low-porosity magma that was emplaced under partly open-system degassing. This conduit stratigraphy gives the vision of a strongly heterogeneous magma column immediately prior to its disruption. The data, however, was sampled among the products of a series of explosions that occurred in 1997, which yielded an average porosity distribution within the conduit. Here, we sampled a single Vulcanian event that occurred on February 11, 2010, to obtain a more accurate snapshot of the porosity distribution in the conduit just prior to explosion.

The February 11 event ended the fifth phase of lava extrusion since the beginning of the current eruption of Soufrière Hills volcano (Stinton et al., 2014a; Stinton et al., 2014b; Wadge et al., 2014b; Cole et al., 2014; Cole et al., 2015). This 4-month period of intense extrusive activity was marked by a succession of dome growth as lava lobes and spines followed by partial dome collapse. Five isolated Vulcanian explosions occurred near the end of this phase. The average extrusion rate during phase 5

was 7 m^3/s with wide variations (Stinton et al., 2014a). A rate of 9 m^3/s was measured over January 12–14, shortly after the most voluminous Vulcanian explosion to date on January 8 (Cole et al., 2014). A rate of 1.2 m^3/s was measured over January 22–28, and a rate of 0.1 m^3/s was measured from January 30 until February 5 when a Vulcanian explosion occurred (Stinton et al., 2014a). Another Vulcanian explosion took place on February 8. Lava extrusion soon resumed on the W side of the dome before changing direction to N a day before February 11, date at which the large Vulcanian explosion studied here took place during the last 20 minutes of the 107-min-long partial dome collapse (Stinton et al. 2014).

The triggering context of the February 11 event is noteworthy. There is a well-established link between magma ascent rate and the occurrence of Vulcanian explosion (Miwa et al., 2009; Degruyter et al., 2012; Cassidy et al., 2015). Despite changes in extrusion rate in the days leading to it, the February 11 event seems to have been driven more by shallow processes than by deeper changes such as an increase of ascent rate and/or of chamber pressure (Stinton et al., 2014b; Cole et al., 2015). This complex event started by generation of pyroclastic density currents that occurred in rapid succession as a result of the collapse of the large dome that was present. The pulsatory Vulcanian explosion ensued the gravitational triggering of the event as a probable result of the unloading of the magma column. This makes the February 11 event an ideal case study to test whether the pre-explosive column was in a state close to that expected for dome-forming, effusive activity and, more broadly, to characterize the state of the volcano prior to a Vulcanian explosion. There is a wealth of information that can be used to characterize such a state because quite a number of studies involving conduit flow modeling that have been conducted at Soufrière Hills focused on its effusive activity (e.g., Melnik and Sparks, 2002; Melnik and Sparks, 2005; Mason et al., 2006; Costa et al., 2007; Collombet, 2009; Kozono and Koyaguchi, 2010; Albino et al., 2011; Costa et al., 2012; Degruyter et al., 2012; Costa et al., 2013). These models have provided first-order constraints on the interplay between ascent rate, volatile exsolution, and outgassing.

The transition between effusive behavior and explosive behavior is closely related to the way the gas phase separates itself from the rest of the ascending magma. There is a complex relationship between magma inflation by volatile exsolution and gas expansion and deflation by permeable flow and outgassing. One important step was to link the magma permeability to the structure and geometry of the bubble network (e.g., Klug et al., 2002; Rust and Cashman, 2004; Wright et al., 2006; Bouvet de Maisonneuve et al., 2009; Wright et al., 2009; Degruyter et al., 2010; Burgisser et al., 2017; Colombier et al., 2017; Vasseur and Wadworth, 2017). Extensive experimental work has shown that bubbles growing in response to decompression may connect each other and form a permeable network when a percolation threshold has been overcome. Such threshold occurs at 30–80 vol.% porosity (e.g., Lindoo et al., 2016). Recently, Burgisser et al. (2017) proposed a permeability relationship that includes a percolation threshold. It was built using experimentally decompressed natural melts and included samples bearing deformed bubbles. Natural samples, however, are permeable at porosities below this percolation threshold because the gas pathways are no longer made of interconnected bubbles. Below 10–15 vol.% porosity, the pathways are made of a network of cracks and permeability drops from ~10^{-14} to <10^{-17} m^2 (Farquharson et al., 2015; Farquharson et al., 2016). While the presence of cracks has been confirmed at shallow depth (Heiken et al., 1988; Castro et al., 2012b; Lavallée et al., 2013; Kendrick et al., 2016), their existence at the depth of several kilometers is more speculative for intermediate and evolved magma compositions because the water dissolved in the melt lowers its viscosity and keeps the brittle behavior out of reach of reasonable strain rates (e.g., Edmonds et al., 2010; Cordonnier et al., 2012). Experiments on porous volcanic rock and magma have shown that ductile behavior can be expected even at shallow depths within the conduit (Heap et al., 2015; Heap et al., 2017).

The relationship between the creation of gas pathways by bubble connection or by brittle behavior of the melt has only started to be addressed (Kushnir et al., 2017). Permeability supported by bubbles is sensitive to the presence of crystals (e.g., Parmigiani et al., 2017) and shear can strongly reorganize the permeable network (e.g., Laumonier et al., 2011; Pistone et al., 2012). Relationships

describing permeability supported by cracks are not easily scaled up from laboratory to conduit characteristic sizes (Farquharson and Wadsworth, 2018). Another obstacle is that permeability has a hysteretic behavior that depends on whether it is being generated by expansion and exsolution of bubbles or by collapse (Rust and Cashman, 2004; Farquharson et al., 2016). In the case of collapse, porosity reduction can be accompanied by permeability reduction if the driving force is shear (Kolzenburg and Russell, 2014) or gravitation (Michaut et al., 2013). Such densification can also occur without significant reduction in permeability if the main mechanism is selective collapse of the smallest vesicles because of surface tension (Kennedy et al., 2016). The complexity of these interactions between crystal-bearing melt and networks of bubbles and cracks is such that there is currently no unified framework to describe magma outgassing at depth.

We first present a combination of textural analyses and glass water content determinations of pumice emitted by the February 11, 2010 Vulcanian explosion that yields pre-explosive values of porosity, pressure, and depth. We then show that some permeability relationships calibrated for high (>15 vol.%) porosity can also be used to empirically represent the behavior of magma permeability at low porosity. We use one of these permeability relationships and a conduit flow model to characterize the pre-explosive conditions of the February 2010 event by fitting model outputs to our data on pre-explosive porosities and pressures.

2. Methods

Twenty-three samples from the February 2010 eruption were collected for analysis (Table S1). Thirteen samples were from pumice-rich pyroclastic density current deposits in Farm River valley (AMO210 label prefix, pumice levee facies on Fig. 7.11 in Stinton et al., 2014b). Ten samples were pumices from fallout deposits at Harris Lookout, Spanish Point, and at White's Bottom Ghaut (WP label prefix, fallout deposits of Stinton et al., 2014b). All samples from fallout and some samples from levee that correspond to the “pumice boulders” of Cole et al. (2015) were texturally homogeneous

pumices. The other levee samples were texturally heterogeneous pumice with some clasts showing macroscopic banding with sharp to lobate or crenulate boundaries between the dense and vesicular parts (Farquharson and Wadsworth, 2018). Only one representative crystalline dense clast was analyzed (AMO210B) because such texture has been shown to originate from to the dome (Burgisser et al., 2010) and our focus was to characterize deeper sourced material.

Small cores ~2 cm^3 were drilled in each pumice. The half of the core closest to the clast surface was discarded so as to avoid weathering effects, while the other half was cut in two, one being subjected to textural analysis and the other being used for H_2O measurement. This procedure ensured that the various analyses characterize the same volume of sample. The size of this volume and the image analysis techniques we used imposed an upper limit to the vesicle size that could be characterized (~1 mm across). As in the 1997 deposits (Giachetti et al., 2010), most pumices produced by the February 11 event that are smaller than ~ 30 cm lack radial gradients in vesicle abundance or size. Some vesicular blocks larger than this exhibit anastomosed regions with vesicles up to several cm, which is well above the sizes our method can measure. Such blocks were avoided in our study to ensure that we obtained representative vesicle size distributions of all analyzed clasts. Drawing from the observations done of the 1997 flows, where similar blocks were sampled closer to the dome to minimize transport-induced breakage (Giachetti et al., 2010), regions with large voids tend to be concentrated in the center of the clasts, which suggest a post-fragmentation origin (i.e. such large voids belong to the syn-explosive, coalesced vesicle population defined below). Avoiding sampling clasts with large voids does not affect the representativeness of our reconstruction of the magma column because the effect of post-fragmentation bubbles is removed by the procedure described below that converts pumice porosities to pre-explosive conditions (Burgisser et al., 2010).

The textural characterization of the samples was done by combining Scanning Electron Microscopy (SEM) and element mapping by Energy Dispersive Spectroscopy (EDS). Polished sections were imaged using a LEO STEREOSCAN 440 (LEICA) SEM operating at 20 kV

accelerating voltage (Université Savoie Mont Blanc) in backscattered electron mode (BSE) to which is attached an EDS probe QUANTAX EDS (Bruker AXS). Images were acquired using the BSE mode (Fig. 1A) and the elements Si, Fe, Mg, Al, and Ca at two different resolutions to ensure that the full range of object sizes was represented. The combination of resolutions was either one image at ×50 and 2 to 3 images at ×1000 for the WP sample suite, or 1 to 2 ×50 images and 4 ×2000 images for the AMO sample suite. Images resolution was such that the respective pixel sizes at magnifications of either ×1000, or ×2000 were identical. The ×50 images of samples AMO210B, G, J, and L were composed by tiling 9 ×100 images, which added a reconstruction uncertainty of 2 vol.% on measured proportions. Instead of SEM images, the ×50 images of samples AMO210D, F, H, and Q were 2D slices of 3D volumes with voxel edge-length of 7–10 μm obtained by X-ray tomography (Phoenix Nanotom 180 at ISTO, Université d'Orléans) following the procedure described in Castro et al. (2012a). In these four samples, oxides and plagioclases were segmented manually from the ferromagnesian minerals based on X-ray attenuation level (Supplementary Fig. S1) and the respective proportions of ferromagnesian minerals were assumed constant at the values provided by Murphy et al. (2000). Images were used to quantify in each sample the amounts of phenocrysts, microlite, vesicles, and glass (Table 1) following the resolution assembly procedure of Giachetti et al. (2010) and the quantification method described in Drignon et al. (2016) (Supplementary Text S1 and Fig. S2).

Glass water contents of the 20 samples listed in Table 2 were measured by using the Flash 2000 elemental analyzer (ISTO, Université d'Orléans). Samples were crushed with an automatic grinder without removing phenocrysts to obtain ~7 mg of powder <30 μm. Following the procedure outlined in Drignon et al. (2016), tin capsules containing the powders were placed in a furnace where they were heated to ~1800°C in the presence of O_2. A helium flux transported the liberated H in H_2O form, which was discriminated from other volatiles by chromatography and analyzed by thermal conductivity. We used the certified standard PYRO (5 wt.% H_2O by Karl Fisher titration, Burgisser et

al., 2010). Total amounts of H given by the elemental analyzer were converted to bulk H_2O content using H and O molar masses (Table 2). Each sample was analyzed three times in order to quantify measurement error. The resulting relative uncertainty is comparable to that of the standard that was analyzed at regular intervals during a measurement day.

Vesicles were subdivided in four populations using the criteria of Giachetti et al. (2010) (Fig. S2). Large, deformed vesicles of equivalent size >300 μm across and circularity <0.2 were divided into two populations. One population was composed of large angular voids existing between crystal fragments that are similar to those observed in the 1997 Vulcanian pumices (Fig. 1B, Giachetti et al., 2010). We assumed that these voids were formed in response to the decompression accompanying the Vulcanian explosion. The other population was composed of the remaining large vesicles, which were considered as pre-explosive vesicles. The third population was composed of small, isolated, and rounded vesicles of equivalent size <50 μm across and circularity >0.4. The fourth population was composed of all the remaining vesicles, which were often interconnected. These last two populations have been interpreted by Giachetti et al. (2010) as having nucleated, grown, and coalesced in a syn-explosive fashion. As our automatic process cannot discriminate between the two first populations, the voids belonging to the first population were visually identified thanks to their association to broken crystals. They were manually assigned to the syn-explosive, connected vesicle population by removing them one by one from the automatically segmented images (Table 2).

The bubble-free vesicles and oxide number densities (i.e. number of objects per unit volume of melt plus crystal) were obtained from the SEM and tomography images using the stereological transformations from Cheng and Lemlich (1983) as explained in Giachetti et al. (2010). Having only two levels of magnifications yields size distributions with artifacts around the cut-off length scale (Supplementary Text S2 and Fig. S4). Total number densities reported in Table 2, however, are dominated by small vesicles and oxides that are below the cut-off scale. As a result, they are not sensitive to such artifacts.

As in Drignon et al. (2016), two physical models were successively used to convert variables measured in the pumice to pre-explosive conditions (Table 3). The first model uses the vesicularities and interstitial glass water contents to estimate pre-explosive pressures and porosities (Burgisser et al., 2010). It has four free parameters (two related to bubble populations, one related to the quench pressure, and one related to outgassing), which combined yield 11 sets of pre-explosive pressures and porosities. The set with the reference values (see *Results* section) of the free parameters was kept as the average set and the two sets with the largest and smallest porosity values at any pressure were kept as extrema to characterize model uncertainty. Analytical uncertainties for each sample were calculated with an additional four sets of outputs that used the average values of the free parameters and the respective minimum and maximum values of glass water content and vesicularity.

Pre-explosive pressures were then converted into pre-explosive depths thanks to the second model (Burgisser et al., 2011). Briefly, each sample is assumed to represent a slice of the magma column and the slice thickness is adjusted so that the pressure at its base due to the overlying load equals that determined by the first model. As in Drignon et al. (2016), two end-members scenarios were considered. The first assumes that pressure is magma-static, i.e. that the pressure in the magma column is created by the sole weight of magma because conduit walls are fully rigid. In the second scenario pressure is lithostatic, which implies that the conduit walls are not rigid. The pressure distribution within the conduit during eruption is, however, expected to be controlled dynamically. The higher the porosity is in the magma, the more the dynamic pressure deviates from a linear trend. Conversely, gas-poor conditions limit dynamic effects. Magma- and lithostatic pressure gradients frame most dynamic pressure distributions in gas-rich conditions (Burgisser et al., 2011). Here, we use the a posteriori argument that the conduit was mostly filled by low-porosity magma to linearly relate pressure and depth.

2.1. Conduit flow modeling

Two permeability relationships were used to quantify gas–melt separation during magma

ascent:

$$k_K = a_K \phi_c^{b_K} \quad (1)$$

$$k_B = \frac{\phi_c^{2.73} d^2}{800} \quad (2)$$

where a_K and b_K are fitting constants, d is the bubble equivalent diameter in m, and ϕ_c is the connected porosity, which is volume of interconnected bubbles that span the entire sample from side to side, divided by the total sample volume. Equation (1) is from Klug and Cashman (1996) and Eq. (2) is from Burgisser et al. (2017) when neglecting bubble deformation and thus assuming spherical bubbles. The bubble equivalent diameter is given by:

$$d^3 = \frac{6\phi_t}{\pi N_T (1 - \phi_t)} \quad (3)$$

where ϕ_t is the total porosity and N_T is the number of bubble per unit volume of melt and crystals. The connected porosity is given by (Burgisser et al., 2017):

$$\phi_c = \frac{\phi_t}{1 + exp\left[c_1 (1.5 \times 10^6 d (\phi_t^{-1/3} - 1) f^{-0.128} - c_2)\right]} \quad (4)$$

where c_1=0.342, c_2= 33.2, and f is the ratio of the standard deviation of the bubble size distribution over d, which is a measure of the degree of polydispersity of the bubble population[1]. The percolation threshold is modeled by setting ϕ_c=0 when the total porosity is below the percolation porosity, ϕ_p:

$$\phi_p = \left[1 + \frac{c_2 + c_3}{1.5 \times 10^6 d} f^{0.128}\right]^{-3} \quad (5)$$

where c_3=6.

Kozono and Koyaguchi (2010) provided a simple algebraic equation that relates pressure and

[1] The equation 19 in Burgisser et al. (2017) should read: $\phi_c = \frac{\phi_t}{1 + exp\left[-c_\phi (1.5 d_a (\phi_t^{-1/3} - 1) f^{-0.128} - c_p)\right]}$

porosity in a volcanic conduit and that approximates a steady state solution of a popular 1D, two-phase conduit flow model (Kozono and Koyaguchi, 2009a; Kozono and Koyaguchi, 2009b; Degruyter et al., 2012; Burgisser et al., 2017). For simplicity, we refer to this simplified formula as the 0D model (Kozono and Koyaguchi, 2010):

$$1 - \frac{n\rho_{mc}RT(1-\phi_t)}{(1-n)P\phi_t}(1-E_w) + \Pi + \frac{1-\phi_t}{1-n}\Theta = 0 \quad (6)$$

$$\Pi = \frac{8\mu_{mc}k_j}{\mu_g r_c^2 \phi_t} \quad (7)$$

$$\Theta = \frac{k_j \rho_{mc}^2 g(1-\phi_t)\pi r_c^2}{\mu_g Q \phi_t} \quad (8)$$

where n is the gas mass-flow rate fraction, μ_g=2×10^{-5} Pa s is the gas viscosity, r_c is the conduit radius in m, g=9.81 m/s^2 is the gravity acceleration, μ_{mc} is the bulk (liquid and crystal) suspension viscosity in Pa s, ρ_{mc} is the bulk (liquid and crystal) density in kg/m^3, T is the temperature in K, P is the pressure in Pa, R=462 J/K kg is the specific gas constant for H_2O gas, k_j is either of k_B or k_K, and Q is the mass flux in kg/s. The parameter E_w is defined as (Kozono and Koyaguchi, 2010):

$$E_w = \frac{\pi r_c^2 q_w}{nQ} \quad (9)$$

where q_w is the flow rate of gas escaping laterally. The gas mass-flow rate fraction is:

$$n = \frac{n_0 - s\sqrt{P}}{1 - s\sqrt{P}} \quad (10)$$

where the initial water content, $n_0 = s\sqrt{\rho_w g L}$, is a function of the conduit length, L, of the solubility constant, s, and of wallrock density, ρ_w=2600 kg/m^3. For comparison purposes, we converted mass fluxes to representative ascent rates by using bubble-free magma density and assuming a constant conduit radius of 15 m (e.g., Wadge et al., 2014b) except where mentioned.

Fitting of five free parameters (Q, r_c, E_w, N_T, and f) was done by minimizing the sum of squared differences between the measured porosities and those given by Eq. (6) for the 19 pre-explosive

pressures determined from sample analysis. The parameter combinations having squared difference falling within the 95% level confidence were considered as plausible solutions. If S_i is the sum of squared differences for a given combination of the free parameters and S_m is the minimum sum of squared differences of the entire parametric sweep, the 95% level of confidence is given by:

$$S_i \leq S_m\left(1 + \frac{p}{o-p}F^{p}_{1-\alpha}{}^{o-p}\right) = 1.1858\, S_m \quad (11)$$

where p=5 is the number of parameters, o=19 is the number of observations, α=0.95 is the level of confidence, and F is the (1-α) quantile of the F distribution with p and (o-p) degrees of freedom.

We set the temperature, T, to 850 °C (Barclay et al., 1998; Murphy et al., 2000) and the liquid phase is considered as a single-phase suspension of silicate melt and crystals with a density, ρ_{mc}, of 2450 kg/m^3 (Burgisser et al., 2011). The effect of dissolved water on melt viscosity followed the relationship by Hess and Dingwell (1996) and the effect of crystals on bulk suspension viscosity, μ_{mc}, was calculated using Krieger and Dougherty (1959) with a maximum packing of 0.65 and an Einstein coefficient of 2.5. The crystal content was set to 55 vol.% based on our data (Text S3, Fig. S5). Such a high value implies that magma rheology is non-Newtonian. Robust rheological relationships of realistic mixtures of phenocrysts and highly elongated microlites are currently not available, but various non-Newtonian approximations of the behavior of crystal-rich suspension have been proposed (e.g., Caricchi et al., 2007; Costa et al., 2009; Mader et al., 2013). In our case, the 0D approximation assumes a Newtonian liquid–wall friction that neglects such effects. This choice is motivated by the fact that our modeling focuses on the effusive regime with low gas volume fraction, which limits the upward acceleration within the conduit.

3. Results

Our samples from the February 11 event have bulk vesicularities of 44–78 vol.% and vesicle-free glass contents of 23–73 vol.%, except AMO210B that has 7.5±2.4 vol.% glass (Table 1). Isolated

syn-explosive vesicles, connected syn-explosive vesicles, and connected pre-explosive vesicles are present in the respective proportions of 1±1.1:87±7.0:12, where the uncertainties have been attributed to the first two bubble populations and the percentage of the last population is such that the three sum to 100% of the total vesicle volume fraction. The pre-explosive vesicles are large, deformed and coalesced. Such textures can be due to deflation occurring either pre-explosively, or syn-explosively. The dominant population of syn-eruptive vesicles, however, displays convex surfaces that suggest net inflation. Many fallout pumices also suggest net inflation because of their bloated shapes. Glass water contents range from 0.4 to 2.2 wt.%, except again AMO210B that has 7.4±2.4 wt.% water (Table 2). The outlier values of AMO210B are due to the very low amount of bulk glass content, 3.6±1.1 vol.%. Considering that glass content is deduced by subtraction, which makes the quantification of small amounts of glass difficult and that AMO210B has a large (14 vol.% bulk) amount of unclassified mineral phases, we decided to leave AMO210B out of the analysis, which then comprises 19 samples. This is consistent with the fact that 7.4 wt.% glass water is much higher than the amount of water thought to be contained in the magmatic reservoir (4.6 wt.%, Barclay et al., 1998).

In using the model that converts vesicularities and interstitial glass water contents to pre-explosive pressures and porosities, a magma temperature of 850 °C and a bubble-free magma density of 2450 kg/m^3 (i.e., melt plus crystals) is assumed (Burgisser et al., 2010). The two free parameters linked to bubble populations were constrained by the proportions of the three vesicle types and their uncertainties. The model assumes that only the pre-explosive vesicles existed in the conduit prior to the explosion and thus that the gas contained in the syn-explosive vesicles was either dissolved in the melt or has been outgassed during the explosion. Following Burgisser et al. (2010), the parameter constraining the amount of overpressure that clasts can sustain was set to the reference value of $1^{-0.5}_{+1}$. The parameter that quantifies outgassing is the ratio between the amount of gas lost by outgassing during magma fragmentation and the total amount of gas present during the explosion. The upper and lower values of this parameter were chosen so that the maximum total water content is <4.6 wt.%, which corresponds to a saturation pressure of 130 MPa (Barclay et al., 1998), and so that all clasts had

net syn-explosive inflation, as suggested by textural observations. These conditions imply that between 10 and 76% of the gas present syn-explosively was outgassed, with an assumed reference value of 50% for this poorly constrained parameter that has a modest effect on pre-explosive pressures.

Figure 2 shows the pre-explosive pressures as a function of the pre-explosive porosities. Clasts originated from 8–70 MPa with porosities from 1 to 10 vol.%. Uncertainties on the porosities are dominated by model assumptions whereas uncertainties in pre-explosive pressures reflect the natural variability of glass content in the samples. The number of samples is large enough to give a representative pressure-porosity distribution but too small to yield a reliable estimate of the upper pre-explosive pressure limit (Drignon et al., 2016). The right vertical axis of Fig. 2 shows approximate pre-explosive depths that suggest a drawdown depth of ~3 km. Depths were estimated thanks to two end-member scenarios of overpressure (magma- and litho-static) in the conduit. There are only small differences between these two scenarios because of the low pre-explosive porosities (Table 3), so a single depth axis with an intrinsic uncertainty of ±5% is used in Fig. 2.

Overall, our data indicate that the single Vulcanian event of February 11 evacuated at least the upper 3 km of a conduit that was filled by a low-porosity, high-crystallinity magma. To have ≤10 vol.% porosity suggests that the magma rising from the reservoir had time to extensively degas during emplacement. One possibility is that the magmatic column was significantly permeable to gas, but such low porosities are generally associated with low permeability values. Another is that magma porosity varied rapidly, which implies that our data captures only a snapshot of the conduit state just prior to explosion. In both cases, there must have been specific conditions that allowed the magma to quickly develop significant permeability while its porosity was increasing in response to decompression and ascent from the magmatic reservoir.

Most bubble-supported permeability relationships depend on magma porosity to first order, and tend towards impermeability when extrapolated at low porosity for natural products of effusive

eruptions (e.g., Mueller et al., 2005; Rust and Cashman, 2011). Figure 3A illustrates that trend for a representative suite of natural samples from dome-forming eruptions at Soufrière Hills volcano and Colima volcano, Mexico (Farquharson et al., 2015; Farquharson et al., 2016; Farquharson and Wadsworth, 2018). There are several reasons for the scatter in the data at a given porosity value. One reason is the 1–2 orders of magnitudes of permeability variation as a function of sample orientation the permeable network is anisotropic. Another reason is the transition from crack-supported permeability at low connected porosity to vesicle-supported permeability at connected porosities larger than ~10 vol.%. Finally, samples have heterogeneities that are large compared to sample size. It has been shown that these two types of permeabilities can be represented with two distinct sets of power-law coefficients (Farquharson et al., 2015; Heap and Kennedy, 2016; Kushnir et al., 2016). The wide data scatter, however, drove us to select the broader approach of representing both types with a single relationship.

Figure 3A shows how the two permeability relationships, k_B and k_K, fit the entire range of the natural data. The relationship k_K is a power law depending on ϕ_c with coefficients that are not directly related to characteristics of the bubble network (a_K =1.1×10^{-11} m^2 and b_K=3.35). The relationship k_B includes information about the bubble network, namely the bubble number density, N_T, and a measure of the spread of the bubble size distribution, f. It yields a good fit of all the data when f is allowed to exceed natural bounds (the best-fit value is f=10$^{10.2}$ with N_T =10$^{12.4}$ m^{-3}). Both relationships can thus *empirically* represent the behavior of magma permeability at low porosity, regardless of geometry (by bubble connections or by brittle behavior of the melt) or generation mechanism (by dilatation or by collapse).

The percolation threshold occurs when ϕ_c/ϕ_t =0.114, which is obtained by setting $\phi_p=\phi_t$ in Eqs. (4–5). As the maximum value of ϕ_t is 1, the maximum value of ϕ_c for bubble percolation is 11.4 vol.%, which corresponds approximately to the boundary between crack- and bubble-supported regimes (Fig. 3A). This threshold does not affect the best-fits of k_K and k_B (i.e. ϕ_t is always >ϕ_p) but it

limits the possibility of reaching permeabilities much higher than those best-fits curves (e.g., $\phi_t<\phi_p$ in most of the gray region of Fig. 3A). If, however, Eq. (5) is neglected (i.e. if ϕ_c is given by Eq. (4) even if $\phi_t<\phi_p$), the whole span of values covered by the data (and the gray region of Fig. 3A) can be represented by k_K or k_B, regardless of permeability type. Here we focus on k_B because it has been calibrated jointly with ϕ_c, but similar conclusions can be drawn by using the simpler form of k_K. The full range of permeabilities covered by the data of Fig. 3A can be represented by k_B when $10^8 \leq N_T \leq 10^{19}$ m^{-3}, $10^{-1} \leq f \leq 10^{12}$, and the percolation threshold is neglected. When used in a conduit flow model as closure relationship, k_K helps characterizing magma ascent dynamics. We fitted outputs of a simplified conduit model to our data of Fig. 2 to provide first-order constraints on the type of permeability and other important parameters such as mass flux and conduit radius.

The 0D model relates conduit pressure to magma porosity and depends on the initial (basal) water content, n_0. Two combinations of conduit length, L, and solubility constant, s, were used so as to obtain $n_0 \approx 4.6$ wt.% ($s=4.11\times10^{-6}$ Pa$^{-1/2}$, $L=5$ km and $s=3.4\times10^{-6}$ Pa$^{-1/2}$, $L=6$ km, respectively). The first combination is consistent with previous work on conduit flow modeling at Soufrière Hills volcano (Collombet, 2009; Degruyter et al., 2012) and the second combination is a fit of s to the Liu et al. (2005) solubility relationship that was used in the processing of our data to reconstruct pre-explosive pressures and porosities (Fig. 2). For a given pair of L and s, five free parameters were selected for a grid search: the mass flux, Q, the conduit radius, r_c, the ratio of lateral gas flow rate to the vertical gas flow rate, E_w, the bubble number density, N_T, and the spread of the bubble size distribution, f. This choice is motivated by the fact that all the other variables of the model, such as T or ρ_{mc}, are known much more accurately than these five parameters. The parameter E_w quantifies how efficiently the gas is evacuated through the conduit walls into the wallrock versus how the gas is transported vertically within the conduit (Kozono and Koyaguchi, 2010). Vanishing E_w values thus imply conduit wall impermeability and large E_w imply high wallrock permeability. The ranges of $10^{-3} \leq Q \leq 10^5$ kg/s, $1 \leq r_c \leq 50$ m, $0 \leq E_w \leq 1$, $10^8 \leq N_T \leq 10^{19}$ m^{-3}, and $10^{-1} \leq f \leq 10^{12}$ were chosen so as to ensure

solutions with a wide gamut of mass fluxes at the vent, conduit wall permeability, and magma permeabilities that cover the data range shown in Fig. 3A. Eleven values were used for each parameter, yielding 1.6×10^5 unique combinations. Another 11-value sweep was done with a narrower range for E_w ($0.8\leq E_w\leq1$) to gain accuracy on this parameter because $E_w<0.8$ systematically yielded poor fits. Parameter combinations that verified Eq. (11) were considered solutions that fit our data (Fig. 2) within the 95% level of confidence.

The grid search results are very similar for the two conduit lengths explored, so we only report those with L=5 km and $s=4.11\times10^{-6}$ Pa$^{-1/2}$ for conciseness. The sum of squared differences at the 95% level of confidence are 1.7×10^{-3}, which is well above the sum of squared differences of the data uncertainties, $\sim10^{-6}$, and below that of the reconstruction model uncertainties, $\sim10^{-2}$. The range of solutions we select as best fits thus produce porosity–pressure curves that are within the range of model uncertainties shown in Fig. 2. All solutions fall within a very narrow range of E_w values (0.9–0.94), which implies that conduit walls must be permeable to gas flow. The four other parameters have more scattered values, except N_T and Q that have strongly correlated values. Figure 4A shows the number of solutions sharing the same pairwise values of N_T and Q. There are, for instance, 53 combinations of r_c, E_w, and f that fit our data within the 95% level of confidence with $N_T = 10^{14.6}$ m^{-3} and $Q = 10^{0.2}$ kg/s, which is represented by a circle of size 53 on Fig. 4A. The solutions parallel a power law, $Q\sim N_T^{-2/3}$, that stems from Eq. (6) and that is made visible because these two parameters are varied over several orders of magnitude. Figure 4B shows the number of solutions sharing the same pairwise values of N_T and f. The presence of a percolation threshold was ignored during the grid search. If such a threshold is taken into account, all the solutions lying below the dashed line of Fig. 4B are no longer valid because gas escape is impossible.

Typical measured densities are 10^{10}– 3×10^{16} m^{-3} for isolated, syn-explosive bubbles and 2×10^8–4×10^{10} m^{-3} for pre-explosive bubbles (Fig. S6). The pre-explosive population represents the lowest expected number densities in the magma column just prior to explosion because it results from the

growth and coalescence of bubbles transported from (and/or nucleated in) the magma reservoir. The syn-explosive population is a reasonable upper estimate of the highest bubble number densities expected to occur in the magma column prior to explosion because it results from the sudden decompression of the column by the explosion, which occurred at a rate larger than that accompanying magma ascent from the reservoir.

The full range of measured N_T is indicated on Fig. 4A, as well as the range of observed extrusion rates, from $10^{4.3}$ kg/s over January 12–14, to $10^{3.5}$ kg/s over January 22–28, and to $10^{2.4}$ kg/s over January 30–February 5. Solutions fitting the observed range of extrusion rate, $10^{2.4}$–$10^{4.3}$ kg/s, comprise a narrow range of N_T ($10^{10.2}$–$10^{11.3}$ m^{-3}) and large f values ($10^{6.8}$–10^{12}, Fig. 4B). Such f values are orders of magnitude above natural vesicle distributions (0.1–10; Burgisser et al., 2017). Conversely, solutions that have N_T values within the observed range, f values within the natural range, and that would be compatible with a percolation threshold correspond to very low mass fluxes ($10^{-2.2}$–$10^{0.67}$ kg/s, Fig. 4A). There are thus two sets of remarkable solutions: one high-flux set that fits observed extrusion rates and that has permeability behavior inconsistent with gas bubbles, and a low-flux set that has Q values well below those observed and that has N_T and f values consistent with bubble-supported permeability.

Each solution defines a curve of porosity vs. permeability. Figure 3A shows the permeability behavior of the high-flux solutions and Fig. 3B shows the permeability behavior of the low-flux solutions. The high-flux set covers the field occupied by most samples, whereas the low-flux set comprises permeabilities that are systematically lower than their natural counterparts at any values of connected porosity.

Conduit evacuation and replenishment must occur on a time scale faster than the travel time stemming from the mass fluxes from the 0D model to be consistent with the model assumption of steady state. The January 8 explosion and the associated conduit evacuation were large enough to disturb the upward flow of magma feeding the dome because it is the largest single Vulcanian

explosion to date (Cole et al., 2014). Steady-state conditions could thus only occur within the month preceding the February 11 explosion. Within that period, the timing of conduit replenishment depends on the observed dome growth rate and on conduit radius.

Observations indicate that lava extrusion was occurring irregularly during the month preceding the explosion (Stinton et al., 2014a). Several studies have suggested that the conduit feeding the current eruption at Soufrière Hills volcano is cylindrical in its upper part but takes the shape of a dike at depth (Costa et al., 2007; Costa et al., 2012). The commonly admitted geometry is a 15-m radius cylinder that extends from the vent down to 2 km to a dike of 5 by 400 m that extends from 2 km down to the reservoir at ~5 km depth. Ascent speed is proportional to conduit area and the dike area is equivalent to a 25-m radius cylinder. The largest suggested value of conduit radius is 40 m from volumetric strain data measured during the 29 July 2008 Vulcanian explosion (Young and Gottsmann, 2015). Figure 5 shows the distance that a parcel of magma could have covered from January 8 to February 11 at the observed rates of extrusion when conduit radii of 15, 25, and 40 m are considered. A conduit of 5 km in length would have been fully replenished within ~15 days after the January 8 explosion for a radius of 15 m, whereas ~12% of the conduit (760 m) would have been replenished during the month between the two explosions for a 40-m radius. The two minor Vulcanian explosions that occurred in the few days before February 11 caused negligible additional vertical movement. Because strong temporal variations of the flux were likely during that period (Odbert et al., 2014), the information conveyed by Fig. 5 is an order-of-magnitude estimate of the conduit replenishment rate.

Conduit evacuation and refilling estimates are helpful to decide which solutions calculated by the 0D model are compatible with steady-state conditions. Notwithstanding the strong dependence on conduit radius, Fig. 5 suggests that ascent times shorter than 2–4 weeks are necessary to ensure steady state. Figure 6 shows the predicted ascent time as a function of conduit radius for the span of high- and low-mass flux solutions, respectively. Both solutions sets comprise the full range of explored conduit radii, but only a small fraction of the 0D model solutions are compatible with steady-state

conditions. These solutions all belong to the high mass flux set and correspond to $Q>10^{3.5}$ kg/s and $r_c<25$ m.

In summary, low mass flux solutions are calculated assuming steady-state conditions that are incompatible with the natural observations but have permeability parameters (N_T and f) consistent with bubble-supported permeability. Conversely, high mass flux solutions assume steady-state conditions that could be compatible with natural observations but have permeability parameters inconsistent with bubble-supported permeability.

4. Discussion

Our data suggest that the February 11 explosion took place while the magmatic column was dense and that it evacuated the upper 3 km of the conduit. The extensively outgassed magmatic column just prior to the explosion can be compared with similar data collected from the 1997 Vulcanian explosion series (Fig. 7). Drawdown depths from 2010 are comparable with the 2.5–3.5 km values inferred for 1997 (Druitt et al., 2002; Burgisser et al., 2011). Porosities deeper than 1 km are <10 vol.% in both cases, but the distribution of shallow porosities differ. The larger porosities, up to 60 vol.%, of the 1997 explosion at shallow level complicate the conversion between pre-explosive pressures and depths, which depend strongly on the presence of overpressures in the conduit. Comparing instead pre-explosive pressures removes the need to assume overpressure mechanisms. The high porosity 1997 data correspond to pressures <10 MPa with a few low-porosity samples <2 MPa, whereas our 2010 data has only one, 10 vol.% sample at <10 MPa. The absence of low porosity cap reflects a sampling bias, as the only dense sample was an outlier left out of our analysis. The absence of >10 vol.% porosity samples in 2010 can be due to a combination of three factors. First, the number of samples is smaller for the 2010 event than for the 1997 events. Second, the 2010 data sampled one explosion, whereas the 1997 data was a random sampling of several explosions. Finally, the shallow parts of the magmatic column could have been more outgassed in 2010 than in 1997.

Several studies have suggested that the conduit feeding the current eruption at Soufrière Hills volcano is cylindrical in its upper part but takes the shape of a dike at depth (see discussion in Wadge et al., 2014b). The sampling depth of both the 1997 explosions (Burgisser et al., 2011) and the 2010 event is 2.5–3.5 km, which is comparable to that of the conduit-dyke junction (~2 km, Wadge et al., 2014b). This geometrical change may adversely affect the kinematics of the decompression front that feeds the Vulcanian explosions, thereby interrupting conduit evacuation.

Dense magmatic columns prior to explosive eruptions have also been inferred at Merapi volcano, Indonesia (Fig. 7). Drignon et al. (2016) suggested low-porosity distributions of <10 vol.% deeper than 1 km prior to the opening and paroxysmal stages of the 2010 Merapi eruption. The drawdown depth is more variable at Merapi (4–10 km) than at Soufrière Hills volcano, but both volcanoes display extensive outgassing at depth. At Soufrière Hills, this creates a puzzling situation because the release of CO_2 during dome growth points to the existence of gas pathways that transfer the gas from the deeper parts of the magmatic system to the surface (Edmonds et al., 2010). The percolation of CO_2 through a poorly vesicular magmatic column is difficult to reconcile with the fact that large permeabilities are promoted in magmas where bubbles are numerous and large enough to form permeable networks (e.g., Burgisser et al., 2017).

In an attempt to quantify how low permeabilities have to be to produce such dense magmatic columns, we used the fact that bubble-based permeability relationships recover to first order the behavior of crack-supported permeability. We focused on k_B and assumed no lower limit for percolation. This relationship recovers the full range of a representative suite of eruptive products. These products, however, correspond to magmas that have undergone decompression, degassing, and outgassing. They are thus are not directly representative of the permeable network at depth. The k_B relationship has been shown to represent the bubble-supported permeability of experimental melts at high pressure (Burgisser et al., 2017). It has not, however, been tested on bubble-supported permeability of crystal-bearing melts (Okumura et al., 2012; Parmigiani et al., 2017) or on crack-

supported permeability under high pressure conditions (Kushnir et al., 2017) because of scaling issues (e.g., Farquharson and Wadsworth, 2018). As a result, we cannot exclude that magma permeability at depth deviates from the trend depicted in Fig. 3. Our first-order approach would thus benefit from future progress on the nature of magma permeability at depth.

The 0D model fits of our pressure and porosity data point to a fairly narrow range of values for the ratio of horizontal to vertical gas flux ($0.9 \leq E_w \leq 0.94$). This is consistent with the expectation that lateral gas escape favors porosity reduction (e.g., Kozono and Koyaguchi, 2012). The importance of wallrock permeability in controlling outgassing has long been pointed out (Jaupart and Allegre, 1991; Taisne and Jaupart, 2008; Farquharson et al., 2015). Recently, Chevalier et al. (2017) have refined this view by suggesting that the lowest of wallrock permeability and horizontal magma permeability controls lateral gas loss. If magma permeability is supported by the bubble network, bubble elongation has the potential to reduce the horizontal permeability to very low values (Klug et al., 2002; Wright et al., 2006; Degruyter et al., 2010; Burgisser et al., 2017), which opens the possibility that such permeability reduction exerts a control on the amount of lateral outgassing that exceeds that of wallrock permeability.

Our model outputs suggest that outgassing of a bubble network can be efficient at low permeabilities provided that magma ascent is slow enough. This general result is consistent with findings from other conduit flow model studies (Kozono and Koyaguchi, 2010; Degruyter et al., 2012). Although such combination of low permeability and ascent rate can explain the pre-explosive porosity distribution within the conduit, it is inconsistent with the extrusion rates and the course of the eruption during the month prior to the February 11 event. Whether due to transient magma flow and to the fact that permeability was not supported by a bubble network, this mismatch make it impossible to obtain an estimate of the number density of the bubbles that nucleated during ascent from the reservoir or, more likely, that were inherited from the reservoir (Edmonds et al., 2014; Edmonds et al., 2015; Edmonds et al., 2016). The only constraint brought by our work is thus that measured number

densities of pre-explosive bubbles (10^8–10^{10} m^{-3}) mark the upper limit of actual number densities because bubbles are expected to rarefy during ascent as coalescence and outgassing proceeds (e.g., Gardner, 2007; Martel and Iacono-Marziano, 2015).

Fits of the 0D model with permeabilities expected from connected gas bubbles feature very small discharge rates that suggest near stalling of the magmatic column just prior to the February 11 explosion. These fits cannot be used quantitatively because the steady state conditions assumed by the model are not consistent with the observations. This opens the possibility that our data represent a snapshot of a transient state of the conduit, such as relatively brief and multiple stalling of the ascending magma (Lensky et al., 2008). Seismic record shows sub-daily activity cycles in the days before February 11 (Stinton et al., 2014b), the last activity peaks before dome collapse occurring every 7–8 h. The last magma stalling could not have occurred over more than a couple of hours before the explosion. Magma outgassing is thus efficient enough to occur in less than a few hours, which is consistent with observations (Rodgers et al., 2016) done over the whole course of the Soufrière Hills eruption. After dome collapse, for instance, outgassing decays in hours to a few days (Edmonds et al., 2003). Hour-long, large outgassing events have been measured (Edmonds and Herd, 2007). These considerations suggest that unsteady flow was likely, which implies that rapid redistribution of porosity can occur over timescales of hours or less. A fruitful research direction would thus be to develop 2D, transient conduit flow models where the processes of degassing and outgassing are fully coupled to test whether the feedbacks between porosity reorganization and permeability development can be that fast.

The high mass flux ($>10^{3.5}$ kg/s) fits of the 0D model with conduit radii <25 m are compatible with steady-state flow within the conduit in the days to weeks prior to February 11 (Stinton et al., 2014a). Calculated permeabilities are $<10^{-13}$ m^2 deeper than 500 m (Figs. 2–3), which are values typical of crack-supported permeability. Cracks have been shown to occur by magma brittle failure, which leads to shear bands (Hale and Wadge, 2008) or stick-slip motion (Costa et al., 2012; Costa et

al., 2013). Such cracks, however, are only likely to occur shallowly (Kendrick et al., 2013). Considering the high crystal volume fraction in the Soufrière Hills magma (Murphy et al., 2000) and the presence of gas in the reservoir, one possibility to explain permeability development at depth and at very low gas volume fraction is the interaction of bubbles and crystals (Parmigiani et al., 2017) in a shearing environment (Laumonier et al., 2011). In the absence of more conclusive evidence, we speculate that this scenario is less likely than that involving transient porosity redistribution.

5. Conclusions

We analyzed pumices from the February 11, 2010 Vulcanian explosion that immediately followed a large dome collapse at Soufrière Hills volcano. We obtained pre-explosive values of porosity, pressure, and depth by combining textural analyses and glass water content determinations. Our data suggest that the February 11 explosion evacuated the upper 3 km of the conduit from the dense (≤10 vol.% porosity) magma it contained. Such drawdown depth is comparable to that inferred for the 1997 Vulcanian explosion series (Burgisser et al., 2010). The low porosity distribution in the volcanic conduit suggests that the magma rising from the reservoir has had time to extensively degas.

We used a conduit flow model to characterize conditions allowing the magma to develop significant permeability and outgassing that counteract the increase in porosity caused by ascent and decompression. We used permeability relationships that were calibrated for high (>15 vol.%) porosity but that also empirically represent the behavior of magma permeability at low porosity, regardless of geometry (by bubble interconnection or by melt fracturing) and generation mechanism (by inflation or by collapse). The conduit flow model is an algebraic equation relating pressure and porosity (Kozono and Koyaguchi, 2010) that approximates steady-state solutions of a 1D two-phase conduit flow model (Kozono and Koyaguchi, 2009b; Degruyter et al., 2012). Model input parameters were fitted so as to match our pre-explosive porosity data, which yielded first-order constraints on conduit radius, mass flux, outgassing efficiency, and permeability.

Model fits point to high ratios of horizontal to vertical gas flux ($0.9 \leq E_w \leq 0.94$). Efficient lateral gas escape is thus necessary to explain the low pre-explosive porosities. Solutions fitting the observed range of lava extrusion rate in the month preceding the February 11 event assume steady-state conditions that could be compatible with natural observations but have permeability parameters inconsistent with bubble-supported permeability. Conversely, solutions with permeability parameters (N_T and f) consistent with bubble-supported permeability are associated to mass fluxes so low that the steady-state assumption is incompatible with the natural observations.

Our modeling suggests two possible scenarios to explain the low pre-explosive porosities. The first possibility is that fast ascent prior to February 11 ensured steady-state conditions, in which case our modeling suggests permeabilities $<10^{-13}$ m^2 deeper than 500 m. These values typical of crack-supported permeability (Farquharson et al., 2015; Farquharson et al., 2016) bring an additional confirmation of the gas pathways at depth that have been inferred from gas measurements at the vent (Edmonds et al., 2003), but the empirical nature of our permeability relationship leaves their genesis unexplained. The second possibility is that transient flow conditions prevailed prior to the February 11 event, in which case our data are a snapshot of the porosity distributions within the conduit that does not preclude much higher porosities to have existed in the conduit. This scenario is consistent with the irregular but active dome growth in the month prior to the February 11 event. In particular, near stalling of the magmatic column and extensive outgassing could have happened at most a couple of hours before dome collapse. Taking into account observations on the degassing patterns over the whole course of Soufrière Hills eruption, this suggests that porosity redistribution can occur over timescales of hours or less.

Acknowledgments

We thank the help of the MVO staff with a special mention to Adam Stinton and Paul Cole for their friendly and highly knowledgeable assistance on the field. Fieldwork would not have been

possible without the help of Mickaël Laumonier and his concern for meat-eating birds. Insightful suggestions from Mike Heap and two anonymous reviewers were of great help to improve this manuscript. This project was partially funded by a grant from Labex OSUG@2020 (Investissements d'avenir – ANR10 LABX56) and grant 202844 from the European Research Council under the European FP7.

References

Albino, F., Pinel, V., Massol, H., Collombet, M., 2011. Conditions for detection of ground deformation induced by conduit flow and evolution. J. Geophys. Res. Solid Earth 116, B06201. https://doi.org/10.1029/2010JB007871

Barclay, J., Rutherford, M.J., Carroll, M.R., Murphy, M.D., Devine, J.D., Gardner, J., Sparks, R.S.J., 1998. Experimental phase equilibria constraints on pre-eruptive storage conditions of the Soufriere Hills magma. Geophys. Res. Lett. 25, 3437–3440.

Bouvet de Maisonneuve, C., Bachmann, O., Burgisser, A., 2009. Characterization of juvenile pyroclasts from the Kos Plateau Tuff (Aegean Arc): insights into the eruptive dynamics of a large rhyolitic eruption. Bull. Volcanol. 71, 643–658. https://doi.org/10.1007/s00445-008-0250-x

Burgisser, A., Arbaret, L., Druitt, T.H., Giachetti, T., 2011. Pre-explosive conduit conditions of the 1997 Vulcanian explosions at Soufrière Hills Volcano, Montserrat: II. Overpressure and depth distributions. J. Volcanol. Geotherm. Res. 199, 193–205.

Burgisser, A., Chevalier, L., Gardner, J.E., Castro, J.M., 2017. The percolation threshold and permeability evolution of ascending magmas. Earth Planet. Sci. Lett. 470, 37–47. https://doi.org/10.1016/j.epsl.2017.04.023

Burgisser, A., Poussineau, S., Arbaret, L., Druitt, T.H., Giachetti, T., Bourdier, J.-L., 2010. Pre-explosive conduit conditions of the 1997 Vulcanian explosions at Soufrière Hills Volcano, Montserrat: I. Pressure and vesicularity distributions. J. Volcanol. Geotherm. Res. 194, 27–41. https://doi.org/10.1016/j.jvolgeores.2010.04.008

Caricchi, L., Burlini, L., Ulmer, P., Gerya, T., Vassalli, M., Papale, P., 2007. Non-Newtonian rheology of crystal-bearing magmas and implications for magma ascent dynamics. Earth Planet. Sci. Lett. 264, 402–419.

Cassidy, M., Cole, P.D., Hicks, K.E., Varley, N.R., Peters, N., Lerner, A.H., 2015. Rapid and slow: Varying magma ascent rates as a mechanism for Vulcanian explosions. Earth Planet. Sci. Lett. 420, 73–84. https://doi.org/10.1016/j.epsl.2015.03.025

Castro, J.M., Burgisser, A., Schipper, C.I., Mancini, S., 2012a. Mechanisms of bubble coalescence in silicic magmas. Bull. Volcanol. 74, 2339–2352. https://doi.org/10.1007/s00445-012-0666-1

Castro, J.M., Cordonnier, B., Tuffen, H., Tobin, M.J., Puskar, L., Martin, M.C., Bechtel, H.A., 2012b. The role of melt-fracture degassing in defusing explosive rhyolite eruptions at volcán Chaitén. Earth Planet. Sci. Lett. 333–334, 63–69. https://doi.org/10.1016/j.epsl.2012.04.024

Cheng, H.C., Lemlich, R., 1983. Errors in the Measurement of Bubble Size Distribution in Foam. Ind. Eng. Chem. Fundam. 22, 105–109. https://doi.org/10.1021/i100009a018

Chevalier, L., Collombet, M., Pinel, V., 2017. Temporal evolution of magma flow and degassing conditions during dome growth, insights from 2D numerical modeling. J. Volcanol. Geotherm. Res. 333–334, 116–133. https://doi.org/10.1016/j.jvolgeores.2017.01.016

Clarke, A.B., Esposti Ongaro, T., Belousov, A., 2015. Vulcanian Eruptions, in: Sigurdsson, H. (Ed.), The Encyclopedia of Volcanoes (Second Edition). Academic Press, Amsterdam, pp. 505–518. https://doi.org/10.1016/B978-0-12-385938-9.00028-6

Clarke, A.B., Stephens, S., Teasdale, R., Sparks, R.S.J., Diller, K., 2007. Petrologic constraints on the decompression history of magma prior to Vulcanian explosions at the Soufrière Hills volcano, Montserrat. J. Volcanol. Geotherm. Res. 161, 261–274. https://doi.org/10.1016/j.jvolgeores.2006.11.007

Cole, P.D., Smith, P.J., Stinton, A.J., Odbert, H.M., Bernstein, M.L., Komorowski, J.C., Stewart, R., 2014. Vulcanian explosions at Soufrière Hills Volcano, Montserrat between 2008 and 2010. Geol. Soc. Lond. Mem. 39, 93–111. https://doi.org/10.1144/M39.5

Cole, P.D., Stinton, A.J., Odbert, H.M., Bonadonna, C., Stewart, R.C., 2015. An inclined Vulcanian explosion and associated products. J. Geol. Soc. 172, 287–293.

https://doi.org/10.1144/jgs2014-099
Collombet, M., 2009. Two-dimensional gas loss for silicic magma flows: toward more realistic numerical models. Geophys. J. Int. 177, 309–318.
Colombier, M., Wadsworth, F. B., Gurioli, L., Scheu, B., Kueppers, U., Di Muro, A., & Dingwell, D. B. (2017). The evolution of pore connectivity in volcanic rocks. Earth and Planetary Science Letters, 462, 99-109.
Cordonnier, B., Caricchi, L., Pistone, M., Castro, J., Hess, K.-U., Gottschaller, S., Manga, M., Dingwell, D.B., Burlini, L., 2012. The viscous-brittle transition of crystal-bearing silicic melt: Direct observation of magma rupture and healing. Geology 40, 611–614.
Costa, A., Caricchi, L., Bagdassarov, N., 2009. A model for the rheology of particle-bearing suspensions and partially molten rocks. Geochem. Geophys. Geosystems 10.
Costa, A., Melnik, O., Sparks, R.S.J., 2007. Controls of conduit geometry and wallrock elasticity on lava dome eruptions. Earth Planet. Sci. Lett. 260, 137–151. https://doi.org/10.1016/j.epsl.2007.05.024
Costa, A., Wadge, G., Melnik, O., 2012. Cyclic extrusion of a lava dome based on a stick-slip mechanism. Earth Planet. Sci. Lett. 337–338, 39–46. https://doi.org/10.1016/j.epsl.2012.05.011
Costa, A., Wadge, G., Stewart, R., Odbert, H., 2013. Coupled subdaily and multiweek cycles during the lava dome eruption of Soufrière Hills Volcano, Montserrat. J. Geophys. Res. Solid Earth 118, 1895–1903. https://doi.org/10.1002/jgrb.50095
Degruyter, W., Bachmann, O., Burgisser, A., 2010. Controls on magma permeability in the volcanic conduit during the climactic phase of the Kos Plateau Tuff eruption (Aegean Arc). Bull. Volcanol. 72, 63–74. https://doi.org/10.1007/s00445-009-0302-x
Degruyter, W., Bachmann, O., Burgisser, A., Manga, M., 2012. The effects of outgassing on the transition between effusive and explosive silicic eruptions. Earth Planet. Sci. Lett. 349–350, 161–170. https://doi.org/10.1016/j.epsl.2012.06.056
Drignon, M.J., Bechon, T., Arbaret, L., Burgisser, A., Komorowski, J.-C., Caroline, M., Hayden, M., Yaputra, R., 2016. Preexplosive conduit conditions during the 2010 eruption of Merapi volcano (Java, Indonesia). Geophys. Res. Lett. 43, 11,595-11,602. https://doi.org/10.1002/2016GL071153
Druitt, T.H., Kokelaar, B.P., 2002. The eruption of Soufriere Hills Volcano, Montserrat, from 1995 to 1999.
Druitt, T.H., Young, S.R., Baptie, B...Bonadonna, C...Calder, E.S., Clarke, A. b., Cole, P.D., Harford, C.L., Herd, R.A., Luckett, R., Ryan, G., Voight, B., 2002. Episodes of cyclic Vulcanian explosive activity with fountain collapse at Soufrière Hills volcano, Montserrat. pp. 281-306 TY2-KW-0.
Edmonds, M., Aiuppa, A., Humphreys, M., Moretti, R., Giudice, G., Martin, R.S., Herd, R.A., Christopher, T., 2010. Excess volatiles supplied by mingling of mafic magma at an andesite arc volcano. Geochem. Geophys. Geosystems 11.
Edmonds, M., Brett, A., Herd, R.A., Humphreys, M.C.S., Woods, A., 2015. Magnetite-bubble aggregates at mixing interfaces in andesite magma bodies. Geol. Soc. Lond. Spec. Publ. 410, 95–121. https://doi.org/10.1144/SP410.7
Edmonds, M., Herd, R.A., 2007. A volcanic degassing event at the explosive-effusive transition. Geophys. Res. Lett. 34. https://doi.org/10.1029/2007GL031379
Edmonds, M., Humphreys, M.C.S., Hauri, E.H., Herd, R.A., Wadge, G., Rawson, H., Ledden, R., Plail, M., Barclay, J., Aiuppa, A., Christopher, T.E., Giudice, G., Guida, R., 2014. Pre-eruptive vapour and its role in controlling eruption style and longevity at Soufrière Hills Volcano. Geol. Soc. Lond. Mem. 39, 291–315. https://doi.org/10.1144/M39.16
Edmonds, M., Kohn, S.C., Hauri, E.H., Humphreys, M.C.S., Cassidy, M., 2016. Extensive, water-rich magma reservoir beneath southern Montserrat. Lithos 252–253, 216–233. https://doi.org/10.1016/j.lithos.2016.02.026

Edmonds, M., Oppenheimer, C., Pyle, D.M., Herd, R.A., Thompson, G., 2003. SO2 emissions from Soufrière Hills Volcano and their relationship to conduit permeability, hydrothermal interaction and degassing regime. J. Volcanol. Geotherm. Res. 124, 23–43.

Farquharson, J., Heap, M.J., Varley, N.R., Baud, P., Reuschlé, T., 2015. Permeability and porosity relationships of edifice-forming andesites: A combined field and laboratory study. J. Volcanol. Geotherm. Res. 297, 52–68. https://doi.org/10.1016/j.jvolgeores.2015.03.016

Farquharson, J.I., Heap, M.J., Lavallée, Y., Varley, N.R., Baud, P., 2016. Evidence for the development of permeability anisotropy in lava domes and volcanic conduits. J. Volcanol. Geotherm. Res. 323, 163–185. https://doi.org/10.1016/j.jvolgeores.2016.05.007

Farquharson, J.I., Wadsworth, F.B., 2018. Upscaling permeability in anisotropic volcanic systems. J. Volcanol. Geotherm. Res. 364, 35–47. https://doi.org/10.1016/j.jvolgeores.2018.09.002

Gardner, J.E., 2007. Bubble coalescence in rhyolitic melts during decompression from high pressure. J. Volcanol. Geotherm. Res. 166, 161–176.

Giachetti, T., Druitt, T.H., Burgisser, A., Arbaret, L., Galven, C., 2010. Bubble nucleation, growth and coalescence during the 1997 Vulcanian explosions of Soufrière Hills Volcano, Montserrat. J. Volcanol. Geotherm. Res. 193, 215–231.

Hale, A.J., Wadge, G., 2008. The transition from endogenous to exogenous growth of lava domes with the development of shear bands. J. Volcanol. Geotherm. Res. 171, 237–257.

Heap, M. J., & Kennedy, B. M. (2016). Exploring the scale-dependent permeability of fractured andesite. Earth and Planetary Science Letters, 447, 139-150.

Heap, M.J., Farquharson, J.I., Baud, P., Lavallée, Y., Reuschlé, T., 2015. Fracture and compaction of andesite in a volcanic edifice. Bull. Volcanol. 77, 55. https://doi.org/10.1007/s00445-015-0938-7.

Heap, M.J., Violay, M., Wadsworth, F.B., Vasseur, J., 2017. From rock to magma and back again: The evolution of temperature and deformation mechanism in conduit margin zones. Earth Planet. Sci. Lett. 463, 92–100. https://doi.org/10.1016/j.epsl.2017.01.021

Heiken, G., Wohletz, K., Eichelberger, J., 1988. Fracture fillings and intrusive pyroclasts, Inyo Domes, California. J. Geophys. Res. Solid Earth 93, 4335–4350. https://doi.org/10.1029/JB093iB05p04335

Hess, K.-U., Dingwell, D.B., 1996. Viscosities of hydrous leucogranitic melts: A non-Arrhenian model. Am. Mineral. 81, 1297–1300.

Jaupart, C., Allegre, C., 1991. Gas content, eruption rate and instabilities of eruption regime in silicic volcanoes. Earth Planet. Sci. Lett. 102, 413–429.

Kendrick, J.E., Lavallée, Y., Hess, K.-U., Heap, M.J., Gaunt, H.E., Meredith, P.G., Dingwell, D.B., 2013. Tracking the permeable porous network during strain-dependent magmatic flow. J. Volcanol. Geotherm. Res. 260, 117–126. https://doi.org/10.1016/j.jvolgeores.2013.05.012

Kendrick, J.E., Lavallée, Y., Varley, N.R., Wadsworth, F.B., Lamb, O.D., Vasseur, J., 2016. Blowing off steam: Tuffisite formation as a regulator for lava dome eruptions. Front. Earth Sci. 4. https://doi.org/10.3389/feart.2016.00041

Kennedy, B.M., Wadsworth, F.B., Vasseur, J., Ian Schipper, C., Mark Jellinek, A., von Aulock, F.W., Hess, K.-U., Kelly Russell, J., Lavallée, Y., Nichols, A.R.L., Dingwell, D.B., 2016. Surface tension driven processes densify and retain permeability in magma and lava. Earth Planet. Sci. Lett. 433, 116–124. https://doi.org/10.1016/j.epsl.2015.10.031

Klug, C., Cashman, K.V., 1996. Permeability development in vesiculating magmas: implications for fragmentation. Bull. Volcanol. 58, 87–100.

Klug, C., Cashman, K.V., Bacon, C.R., 2002. Structure and physical characteristics of pumice from the climactic eruption of Mount Mazama (Crater Lake), Oregon. Bull. Volcanol. 64, 486–501.

Kolzenburg, S., Russell, J.K., 2014. Welding of pyroclastic conduit infill: A mechanism for cyclical explosive eruptions. J. Geophys. Res. Solid Earth 119, 5305–5323. https://doi.org/10.1002/2013JB010931

Kozono, T., Koyaguchi, T., 2012. Effects of gas escape and crystallization on the complexity of

conduit flow dynamics during lava dome eruptions. J. Geophys. Res. 117.
Kozono, T., Koyaguchi, T., 2010. A simple formula for calculating porosity of magma in volcanic conduits during dome-forming eruptions. Earth Planets Space 62, 483–488.
Kozono, T., Koyaguchi, T., 2009a. Effects of relative motion between gas and liquid on 1-dimensional steady flow in silicic volcanic conduits: 1. An analytical method. J. Volcanol. Geotherm. Res. 180, 21–36.
Kozono, T., Koyaguchi, T., 2009b. Effects of relative motion between gas and liquid on 1-dimensional steady flow in silicic volcanic conduits: 2. Origin of diversity of eruption styles. J. Volcanol. Geotherm. Res. 180, 37–49.
Krieger, I.M., Dougherty, T.J., 1959. A mechanism for non-Newtonian flow in suspensions of rigid spheres. Trans. Soc. Rheol. III, 137–152.
Kushnir, A.R.L., Martel, C., Bourdier, J.-L., Heap, M.J., Reuschlé, T., Erdmann, S., Komorowski, J.-C., Cholik, N., 2016. Probing permeability and microstructure: Unravelling the role of a low-permeability dome on the explosivity of Merapi (Indonesia). J. Volcanol. Geotherm. Res. 316, 56–71. https://doi.org/10.1016/j.jvolgeores.2016.02.012
Kushnir, A.R.L., Martel, C., Champallier, R., Arbaret, L., 2017. In situ confirmation of permeability development in shearing bubble-bearing melts and implications for volcanic outgassing. Earth Planet. Sci. Lett. 458, 315–326. https://doi.org/10.1016/j.epsl.2016.10.053
Laumonier, M., Arbaret, L., Burgisser, A., Champallier, R., 2011. Porosity redistribution enhanced by strain localization in crystal-rich magmas. Geology 39, 715–718. https://doi.org/10.1130/G31803.1
Lavallée, Y., Benson, P.M., Heap, M.J., Hess, K.-U., Flaws, A., Schillinger, B., Meredith, P.G., Dingwell, D.B., 2013. Reconstructing magma failure and the degassing network of dome-building eruptions. Geology 41, 515–518.
Lensky, N.G., Sparks, R.S.J., Navon, O., Lyakhovsky, V., 2008. Cyclic activity at Soufrière Hills Volcano, Montserrat: degassing-induced pressurization and stick-slip extrusion. pp. 169-188 TY2-KW-0.
Lindoo, A., Larsen, J.F., Cashman, K.V., Dunn, A.L., Neill, O.K., 2016. An experimental study of permeability development as a function of crystal-free melt viscosity. Earth Planet. Sci. Lett. 435, 45–54. https://doi.org/10.1016/j.epsl.2015.11.035
Liu, Y., Zhang, Y., Behrens, H., 2005. Solubility of H2O in rhyolitic melts at low pressures and a new empirical model for mixed H2O-CO2 solubility in rhyolitic melts. J. Volcanol. Geotherm. Res. 143, 219–235.
Mader, H.M., Llewellin, E.W., Mueller, S.P., 2013. The rheology of two-phase magmas: A review and analysis. J. Volcanol. Geotherm. Res. 257, 135–158. https://doi.org/10.1016/j.jvolgeores.2013.02.014
Martel, C., Iacono-Marziano, G., 2015. Timescales of bubble coalescence, outgassing, and foam collapse in decompressed rhyolitic melts. Earth Planet. Sci. Lett. 412, 173–185. https://doi.org/10.1016/j.epsl.2014.12.010
Mason, R.M., Starostin, A.B., Melnik, O.E., Sparks, R.S.J., 2006. From Vulcanian explosions to sustained explosive eruptions: The role of diffusive mass transfer in conduit flow dynamics. J. Volcanol. Geotherm. Res. 153, 148–165.
Melnik, O., Sparks, R.S.J., 2005. Controls on conduit magma flow dynamics during lava dome building eruptions. J. Geophys. Res. 110.
Melnik, O., Sparks, R.S.J., 2002. Dynamics of magma ascent and lava extrusion at Soufrière Hills Volcano, Montserrat. Geol. Soc. Lond. Mem. 21, 153–171. https://doi.org/10.1144/GSL.MEM.2002.021.01.07
Michaut, C., Ricard, Y., Bercovici, D., Sparks, R.S.J., 2013. Eruption cyclicity at silicic volcanoes potentially caused by magmatic gas waves. Nat. Geosci. 6, 856–860.
Miwa, T., Toramaru, A., Iguchi, M., 2009. Correlations of volcanic ash texture with explosion earthquakes from vulcanian eruptions at Sakurajima volcano, Japan. J. Volcanol. Geotherm.

Res. 184, 473–486.
Mueller, S., Melnik, O., Spieler, O., Scheu, B., Dingwell, D.B., 2005. Permeability and degassing of dome lavas undergoing rapid decompression: An experimental determination. Bull. Volcanol. 67, 526–538.
Mueller, S., Scheu, B., Kueppers, U., Spieler, O., Richard, D., Dingwell, D.B., 2011. The porosity of pyroclasts as an indicator of volcanic explosivity. J. Volcanol. Geotherm. Res. 203, 168–174. https://doi.org/10.1016/j.jvolgeores.2011.04.006
Murphy, M.D., Sparks, R.S.J., Barclay, J., Carroll, M.R., Brewer, T.S., 2000. Remobilization of andesite magma by intrusion of mafic magma at the Soufriere Hills Volcano, Montserrat, West Indies. J. Petrol. 41, 21–42.
Odbert, H.M., Stewart, R.C., Wadge, G., 2014. Cyclic phenomena at the Soufrière Hills Volcano, Montserrat. Geol. Soc. Lond. Mem. 39, 41–60. https://doi.org/10.1144/M39.2
Okumura, S., Nakamura, M., Nakano, T., Uesugi, K., Tsuchiyama, A., 2012. Experimental constraints on permeable gas transport in crystalline silicic magmas. Contrib. Mineral. Petrol. 164, 493–501.
Parmigiani, A., Degruyter W., Leclaire S., Huber C., Bachmann O., 2017. The mechanics of shallow magma reservoir outgassing. Geochem. Geophys. Geosystems 18, 2887–2905. https://doi.org/10.1002/2017GC006912
Pistone, M., Caricchi, L., Ulmer, P., Burlini, L., Ardia, P., Reusser, E., Marone, F., Arbaret, L., 2012. Deformation experiments of bubble- and crystal-bearing magmas: Rheological and microstructural analysis. J. Geophys. Res. 117.
Rodgers, M., Smith, P.J., Mather, T.A., Pyle, D.M., 2016. Quiescent-explosive transitions during dome-forming volcanic eruptions: Using seismicity to probe the volcanic processes leading to the 29 July 2008 vulcanian explosion of Soufrière Hills Volcano, Montserrat. J. Geophys. Res. Solid Earth 121, 8453–8471. https://doi.org/10.1002/2016JB013180
Rust, A.C., Cashman, K.V., 2011. Permeability controls on expansion and size distributions of pyroclasts. J. Geophys. Res. 116.
Rust, A.C., Cashman, K.V., 2004. Permeability of vesicular silicic magma: inertial and hysteresis effects. Earth Planet. Sci. Lett. 228, 93–107.
Spieler, O., Kennedy, B., Kueppers, U., Dingwell, D.B., Scheu, B., Taddeucci, J., 2004. The fragmentation threshold of pyroclastic rocks. Earth Planet. Sci. Lett. 226, 139–148.
Stinton, A.J., Cole, P.D., Odbert, H.M., Christopher, T., Avard, G., Bernstein, M., 2014a. Dome growth and valley fill during Phase 5 (8 October 2009–11 February 2010) at the Soufrière Hills Volcano, Montserrat. Geol. Soc. Lond. Mem. 39, 113–131. https://doi.org/10.1144/M39.6
Stinton, A.J., Cole, P.D., Stewart, R.C., Odbert, H.M., Smith, P., 2014b. The 11 February 2010 partial dome collapse at Soufrière Hills Volcano, Montserrat. Geol. Soc. Lond. Mem. 39, 133–152. https://doi.org/10.1144/M39.7
Taisne, B., Jaupart, C., 2008. Magma degassing and intermittent lava dome growth. Geophys. Res. Lett. 35.
Vasseur, J., & Wadsworth, F. B. (2017). Sphere models for pore geometry and fluid permeability in heterogeneous magmas. Bulletin of Volcanology, 79(11), 77.
Wadge, G., Robertson, R.E.A., Voight, B., 2014a. The Eruption of Soufriere Hills Volcano, Montserrat from 2000 to 2010. Geological Society of London.
Wadge, G., Voight, B., Sparks, R.S.J., Cole, P.D., Loughlin, S.C., Robertson, R.E.A., 2014b. An overview of the eruption of Soufrière Hills Volcano, Montserrat from 2000 to 2010. Geol. Soc. Lond. Mem. 39, 1–40. https://doi.org/10.1144/M39.1
Williamson, B.J., Di Muro, A., Horwell, C.J., Spieler, O., Llewellin, E.W., 2010. Injection of vesicular magma into an andesitic dome at the effusive–explosive transition. Earth Planet. Sci. Lett. 295, 83–90. https://doi.org/10.1016/j.epsl.2010.03.027
Wright, H.M.N., Cashman, K.V., Gottesfeld, E.H., Roberts, J.J., 2009. Pore structure of volcanic

clasts: Measurements of permeability and electrical conductivity. Earth Planet. Sci. Lett. 280, 93–104.
Wright, H.M.N., Roberts, J.J., Cashman, K.V., 2006. Permeability of anisotropic tube pumice: Model calculations and measurements. Geophys. Res. Lett. 33.
Young, N.K., Gottsmann, J., 2015. Shallow crustal mechanics from volumetric strain data: Insights from Soufrière Hills Volcano, Montserrat. J. Geophys. Res. Solid Earth 120, 1559–1571. https://doi.org/10.1002/2014JB011551

Figure Captions

Fig. 1: Representative pumice from the 2010 event. A) SEM image (BSE) with a red frame surrounding the region selected for textural analysis to avoid corners affected by the vignetting sometimes occurring at ×50 magnification. B) Analyzed region showing the different analyzed objects: oxides (red), plagioclases (green), orthopyroxenes (cyan), clinopyroxenes and amphiboles (blue), matrix (yellow), vesicles with circularity <0.2 and equivalent size >300 μm (grey), and other vesicles (black). All objects were discriminated by chemical (EDS) mapping except the large, deformed vesicles that were manually outlined.

Fig. 2: Pre-explosive magmatic columns represented by porosity as a function of pressure and depth. Triangles indicate the average model outputs for each sample, grey areas cover the ranges of outputs of the 10 parametric model runs, and error bars represent the combined effects of natural variability and analytical uncertainty on each sample. The solid black curve indicates closed-system degassing if the pure water saturation pressure is 130 MPa.

Fig. 3: Permeability as a function of connected porosity for various input parameters of two relationships (k_B and k_K). Data are from natural products of dome-forming eruptions at Colima volcano (diamonds, Farquharson et al., 2015; Farquharson et al., 2016) and Soufrière Hills (triangles, Farquharson and Wadsworth, 2018). Black-filled symbols indicate permeability values in the direction parallel to gas channels (vesicles or cracks),

white-filled symbols indicate permeabilities perpendicular to gas channels, and gray-filled symbols indicate permeabilities measured regardless of orientation. The limit between crack- and bubble-supported permeability is from Farquharson et al. (2015) and Kushnir et al. (2016). It also corresponds approximately to the percolation threshold (see text). A) The grey area covers the span of curves that correspond to high mass flux solutions. It is bounded by curves with the highest (dashed line) and lowest (solid line) values of bubble number density (N_T), respectively. The thick continuous curve is the best-fit of all the data for k_K and the dotted curve is the best-fit for k_B. B) The grey area covers the span of curves that correspond to low mass flux solutions. It is bounded by curves with the highest (dashed line) and lowest (solid line) values of bubble number density (N_T), respectively.

Fig. 4: Solutions of the five-parameters sweep that fall within the 95% level of confidence. Circle sizes are proportional to the number of solutions that have identical values for the parameter pairs represented by graph axes but different combinations of the three other parameters. Circles are colored according to whether they represent high-flux solutions ($10^{2.4}$–$10^{4.3}$ kg/s, black), low-flux solutions ($10^{-0.6}$–10 kg/s, white), or other solutions (grey) that fit neither the observed extrusion rates nor the measured values of N_T and f. A) Bubble number density (N_T) as a function of mass flux (Q). Grey bars indicate the range of values measured by photogrammetry (x-axis) and by textural analysis (y-axis). The dashed line indicates the slope of the relationship between Q and N_T given by Eq. (6). B) Bubble number density (N_T) as a function of the spread in bubble sizes (f). The dashed line marks the limit between solutions that are compatible with a percolation threshold ("yes") and the solutions that ignore the percolation threshold ("no").

Fig. 5: Distance covered by a parcel of magma between the explosions of January 8 and February 11. Curves are calculated by linear interpolation between the observed average

rates of extrusion (Stinton et al., 2014a) and assuming various constant conduit radii (15, 25, and 40 m). Stars mark explosion times, and the horizontal dashed line is set at the inferred conduit length of 5 km.

Fig. 6: Magma ascent time from the reservoir to the surface as a function of conduit radius. Curves are labeled according to the value of mass flux. The dark grey area covers the ascent rates that are compatible with steady-state conduit replenishment. Light grey areas span combinations of mass fluxes and conduit radius that are solutions of the 0D model. Cases of high and low mass flux solutions are indicated by the labels "high Q" and "low Q", respectively.

Fig. 7: Comparison of different pre-explosive magmatic columns represented by porosity as a function of pressure. Merapi data are from Drignon et al. (2016). Soufrière Hills Volcano (SHV) data are from Clarke et al. (2007) as reanalyzed by Burgisser et al. (2010) and from Burgisser et al. (2010) (label "1997a"), from Williamson et al. (2010) (label "1997b"), and this study (label "Feb. 11, 2010").

Tables

Table 1: Sample phase proportions in vol.%. Values in parenthesis are one standard deviation, not analyzed is "n.a.", and not detected is "n.d.". Abbreviations OPx, CPx+A, and Plag respectively mean orthopyroxene, clinopyroxene plus amphibole, and plagioclase.

Sample	Vesicle	Oxide [a]	OPx [a]	CPx+A [a]	Plag [a]	Glass [a]	Quartz [a]	Other [a]
AMO210A	65.3 (1.0)	1.5 (0.9)	5.3 (0.8)	8.9 (0.1)	38.6 (5.5)	45.6 (6.8)	n.d.	n.d.
AMO210B	51.8 (1.6)	3.5 (0.8)	10.1 (0.7)	5.1 (0.4)	38.3 (1.6)	7.5 (2.4)	7.3 (2.4)	28.3 (1.7)
AMO210C	67.8 (1.4)	1.2 (1.5)	2.9 (1.0)	8.4 (7.7)	46 (12)	45 (12)	n.d.	n.d.
AMO210D	54.5 (3.1)	1.9 (1.2)	2.3 (1.0) [b]	4.9 (2.1) [b]	30.3 (3.5)	60.7 (4.8)	0 [b]	0 [b]
AMO210E	71.0 (0.2)	3.9 (2.2)	20.3 (0.8)	7.4 (4.6)	36.2 (3.8)	31.2 (4.0)	n.d.	n.d.
AMO210F	61.5 (1.1)	2.2 (0.4)	4.8 (1.1) [b]	10.0 (2.3) [b]	48.7 (5.3)	34.4 (1.9)	0 [b]	0 [b]
AMO210G	43.5 (5.2)	1.8 (0.1)	7.7 (2.7)	4.7 (1.9)	26.6 (4.9)	37.4 (6.7)	1.1 (0.1)	20.7 (1.2)
AMO210H	55.6 (4.2)	2.8 (1.6)	5.9 (1.3) [b]	12.4 (2.8) [b]	43.4 (5.6)	35.5 (6.5)	0 [b]	0 [b]
AMO210I	59.7 (1.4)	2.4 (2.8)	11.7 (1.0)	3.9 (0.8)	53.8 (9.9)	27.9 (9.3)	n.d.	n.d.
AMO210J	60.1 (2.0)	6.0 (1.1)	4.4 (3.6)	16.0 (0.1)	35.4 (1.9)	23.4 (1.5)	0.2 (0.1)	14.5 (1.0)
AMO210K	73.6 (0.7)	4.1 (4.5)	1.9 (1.2)	1.8 (0.3)	53 (11)	39.2 (7.5)	n.d.	n.d.
AMO210L	63.5 (2.0)	4.0 (0.3)	5.7 (1.2)	8.5 (1.3)	39.5 (4.1)	23.2 (3.9)	0.3 (0.2)	18.7 (0.8)
AMO210Q	69.8 (0.9)	1.3 (0.4)	1.5 (0.7) [b]	3.1 (1.5) [b]	34.2 (5.9)	59.9 (4.5)	0 [b]	0 [b]
WP1.095A	71.7 (0.3)	2.0 (0.1)	5.1 (2.0)	5.4 (3.3)	39.3 (1.1)	48.2 (0.9)	n.d.	n.d.
WP1.095B	56.6 (0.1)	2.4 (0.5)	7.4 (0.7)	4.3 (3.6)	44.6 (4.1)	41.2 (6.7)	n.d.	n.d.
WP1.108A	62.9 (0.2)	3.0 (1.0)	3.1 (0.5)	1.7 (0.3)	44.1 (5.0)	47.9 (4.7)	n.d.	n.d.
WP1.108B	77.4 (0.8)	1.1 (0.1)	2.3 (0.1)	5.2 (0.4)	39.5 (1.2)	51.7 (3.0)	n.d.	n.d.
WP2.200A	77.1 (0.2)	1.2 (0.04)	10 (10)	7.6 (0.1)	44.5 (6.1)	36.6 (3.6)	n.d.	n.d.
WP2.200B	74.5 (0.5)	3.6 (1.0)	1.6 (0.1)	2.2 (0.4)	34.6 (0.6)	57.9 (2.8)	n.d.	n.d.
WP2.201A	76.7 (0.1)	1.5 (1.4)	2.0 (0.7)	3.0 (3.5)	52.2 (3.7)	41.3 (3.7)	n.d.	n.d.
WP2.201B	77.8 (0.1)	0.3 (0.4)	3.1 (1.6)	4.0 (2.7)	43.5 (0.4)	49.2 (4.8)	n.d.	n.d.
WP2.329A	58.4 (0.7)	2.2 (1.0)	4.3 (1.8)	11.2 (0.3)	9.0 (3.6)	73.2 (5.7)	n.d.	n.d.
WP2.329B	70.6 (1.1)	2.5 (0.7)	37.3 (0.4)	4.3 (0.4)	20.6 (1.3)	34.7 (2.4)	n.d.	n.d.

[a] Bubble-free values.

[b] Small magnification image was a slice from a tomography scan. Values were determined by assuming that all the segmented minerals minus plagioclases and oxides were ferromagnesian minerals and using the ratio (CPx+A)/(CPx+A+OPx) =0.68 and OPx/(CPx+A+OPx) =0.32 (Murphy et al., 2000).

Table 2: Sample glass water contents and textural characteristics. Values in parenthesis are one standard deviation. Columns "Syn isol", "Syn conn", and "Pre conn" respectively represent the proportions (to 100%) of syn-explosive and isolated vesicles, syn-explosive and connected vesicles, and pre-explosive and connected vesicles. Not analyzed is "n.a." and N_T are bubble-free number densities.

Sample	H_2O bulk (wt.%)	H_2O glass (wt.%)	Syn isol	Syn conn	Pre Conn	Bubble N_T (m^{-3})	Oxide N_T (m^{-3})
AMO210A	0.89 (0.049)	1.64 (0.33)	0.9	91.0	8.1	3.6×10^{15} (1.2×10^{14})	2.1×10^{18} (5.3×10^{16})
AMO210B	0.56 (0.031)	7.43 (2.44)	1.3	94.0	4.7	1.2×10^{16} (4.6×10^{14})	1.1×10^{17} (3.7×10^{15})
AMO210C	1.03 (0.057)	1.97 (0.83)	1.2	87.1	11.7	1.5×10^{16} (4.0×10^{14})	1.1×10^{16} (5.0×10^{14})
AMO210D	0.55 (0.030)	0.75 (0.14)	2.1	94.3	3.6	1.5×10^{16} (4.2×10^{14})	1.3×10^{17} (4.4×10^{15})
AMO210E	0.70 (0.077)	2.03 (0.59)	0.4	82.0	17.6	2.0×10^{16} (6.2×10^{14})	1.1×10^{17} (4.5×10^{15})
AMO210F	0.69 (0.049)	1.47 (0.29)	1.5	92.3	6.2	2.2×10^{16} (6.2×10^{14})	1.1×10^{17} (4.4×10^{15})
AMO210G	0.74 (0.041)	1.99 (0.46)	2.1	89.2	8.7	1.2×10^{16} (3.3×10^{14})	1.1×10^{17} (4.0×10^{15})
AMO210H	0.52 (0.029)	0.73 (0.31)	1.0	83.4	15.6	3.8×10^{16} (7.7×10^{14})	2.4×10^{17} (6.5×10^{15})
AMO210I	n.a.	n.a.	n.a.	n.a.	n.a.	2.3×10^{16} (6.0×10^{14})	1.9×10^{17} (5.9×10^{15})
AMO210J	n.a.	n.a.	n.a.	n.a.	n.a.	3.2×10^{16} (8.2×10^{14})	3.7×10^{17} (1.0×10^{16})
AMO210K	n.a.	n.a.	n.a.	n.a.	n.a.	1.3×10^{16} (3.5×10^{14})	1.2×10^{17} (4.1×10^{15})
AMO210L	0.55 (0.030)	1.88 (0.41)	0.2	92.2	7.6	1.6×10^{16} (4.2×10^{14})	4.9×10^{17} (1.8×10^{16})
AMO210Q	1.00 (0.055)	1.63 (0.22)	0.4	86.1	13.5	7.7×10^{15} (1.8×10^{14})	3.2×10^{17} (9.4×10^{15})
WP1.095A	0.55 (0.030)	0.95 (0.20)	0.5	89.8	9.6	1.9×10^{16} (4.4×10^{14})	3.9×10^{16} (1.6×10^{15})
WP1.095B	0.44 (0.024)	0.89 (0.29)	0.9	82.8	16.2	2.1×10^{16} (5.3×10^{14})	5.3×10^{16} (2.0×10^{15})
WP1.108A	0.66 (0.019)	1.41 (0.18)	0.7	88.8	10.5	1.5×10^{16} (3.9×10^{14})	2.5×10^{17} (6.8×10^{15})
WP1.108B	1.12 (0.027)	2.05 (0.15)	0.3	67.0	32.7	1.4×10^{16} (3.1×10^{14})	8.9×10^{16} (2.4×10^{15})
WP2.200A	0.56 (0.031)	1.16 (0.29)	0.3	92.5	7.3	1.5×10^{16} (4.3×10^{14})	2.9×10^{17} (8.8×10^{15})
WP2.200B	0.65 (0.023)	1.11 (0.08)	0.2	92.2	7.6	3.1×10^{16} (4.9×10^{14})	6.1×10^{15} (3.1×10^{14})
WP2.201A	0.54 (0.035)	1.20 (0.28)	0.2	87.6	12.2	2.7×10^{16} (5.6×10^{14})	3.8×10^{16} (1.4×10^{15})
WP2.201B	1.09 (0.11)	2.16 (0.39)	0.1	88.1	11.8	2.0×10^{16} (4.2×10^{14})	6.1×10^{15} (2.3×10^{14})
WP2.329A	0.56 (0.004)	0.43 (0.07)	0.3	73.0	26.7	4.7×10^{16} (7.0×10^{14})	1.2×10^{17} (3.4×10^{15})
WP2.329B	0.55 (0.005)	1.59 (0.13)	0.1	89.6	10.3	2.6×10^{16} (4.2×10^{14})	9.5×10^{16} (2.9×10^{15})

Table 3: Results on the pre-explosive conduit conditions. Values in parenthesis are one standard deviation and the plus and minus signs indicate positive and negative errors. Total gas is the total amount of syn-explosive gas. Depths are measured from the vent down and are considering respectively magma-static (Magm. depth) and litho-static (Lith. depth) conduit pressure gradient.

Sample	Melt H_2O (wt%)	Pressure (MPa)	Porosity (vol.%)	Total gas (wt%)	Magm. depth (km)	Lith. depth (km)
AMO210A	2.27 (0.32)	38.7 (+9.3,-10.3)	2.818 (0.027)	0.73	1.7	1.5
AMO210C	2.65 (0.82)	50.8 (+24.7,-30.7)	2.331 (0.038)	0.79	2.2	2.0
AMO210D	1.23 (0.14)	12.7 (+2.5,-2.8)	6.243 (0.061)	0.55	0.6	0.5
AMO210E	2.79 (0.58)	55.6 (+18.9,-21.8)	2.370 (0.007)	0.88	2.4	2.2
AMO210F	2.04 (0.29)	31.9 (+7.8,-8.6)	3.070 (0.028)	0.66	1.4	1.2
AMO210G	2.37 (0.45)	41.7 (+13.2,-15.1)	1.603 (0.049)	0.44	1.8	1.6
AMO210H	1.22 (0.31)	12.5 (+5.2,-6.4)	6.505 (0.081)	0.57	0.6	0.5
AMO210L	2.48 (0.41)	45.3 (+12.5,-14.1)	2.300 (0.047)	0.69	2.0	1.8
AMO210Q	2.36 (0.22)	41.4 (+6.6,-7.1)	3.029 (0.029)	0.84	1.8	1.6
WP1.095A	1.73 (0.19)	23.7 (+4.6,-5.0)	5.504 (0.006)	0.89	1.1	0.9
WP1.095B	1.40 (0.29)	16.1 (+5.6,-6.7)	5.258 (0.002)	0.58	0.7	0.6
WP1.108A	2.00 (0.18)	30.7 (+4.7,-5.1)	3.290 (0.005)	0.68	1.4	1.2
WP1.108B	3.02 (0.15)	64.0 (+5.4,-5.6)	2.637 (0.033)	1.12	2.8	2.5
WP2.200A	2.12 (0.29)	34.3 (+7.9,-8.8)	4.756 (0.006)	1.11	1.5	1.3
WP2.200B	1.98 (0.08)	30.3 (+2.2,-2.3)	4.821 (0.015)	1.00	1.4	1.2
WP2.201A	2.15 (0.28)	35.2 (+7.8,-8.6)	4.570 (0.004)	1.09	1.6	1.4
WP2.201B	3.15 (0.38)	68.8 (+14.0,-15.2)	2.508 (0.005)	1.15	3.0	2.7
WP2.329A	0.96 (0.07)	8.0 (+1.0,-1.1)	10.436 (0.003)	0.60	0.4	0.3
WP2.329B	2.34 (0.12)	40.8 (+3.8,-3.9)	3.154 (0.035)	0.86	1.8	1.6

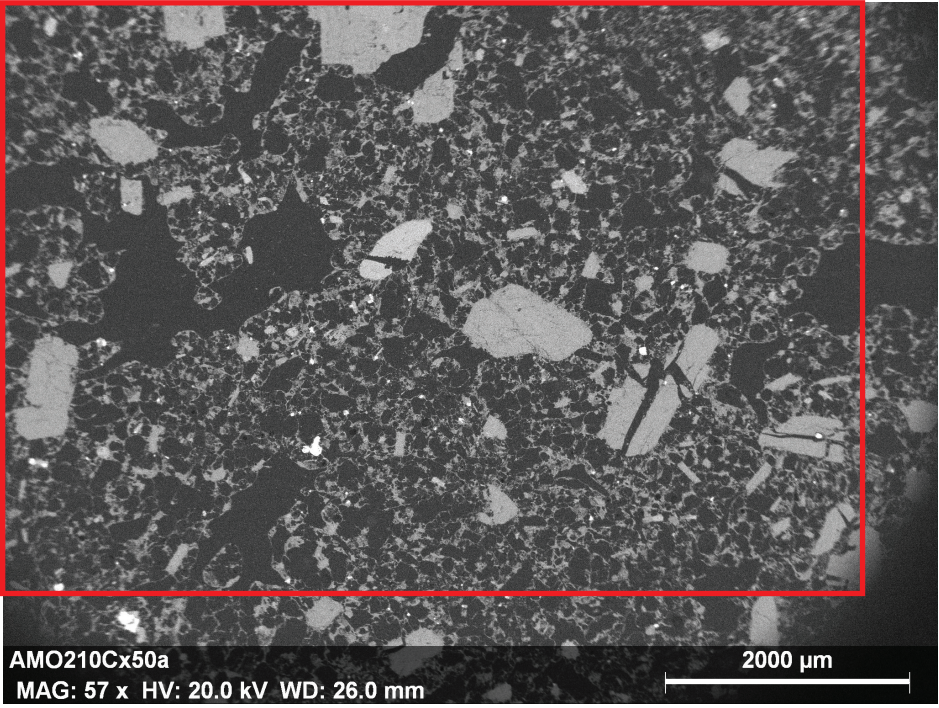

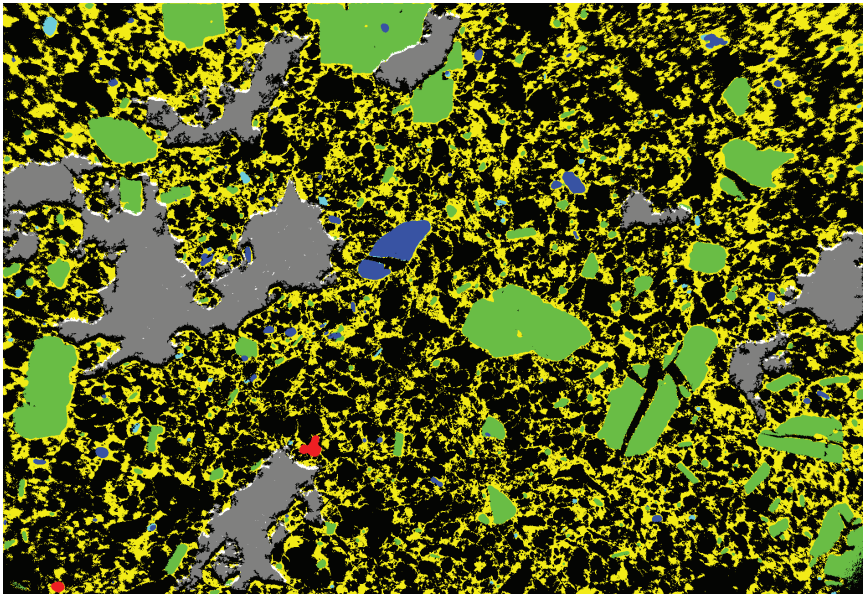

FIGURE 1

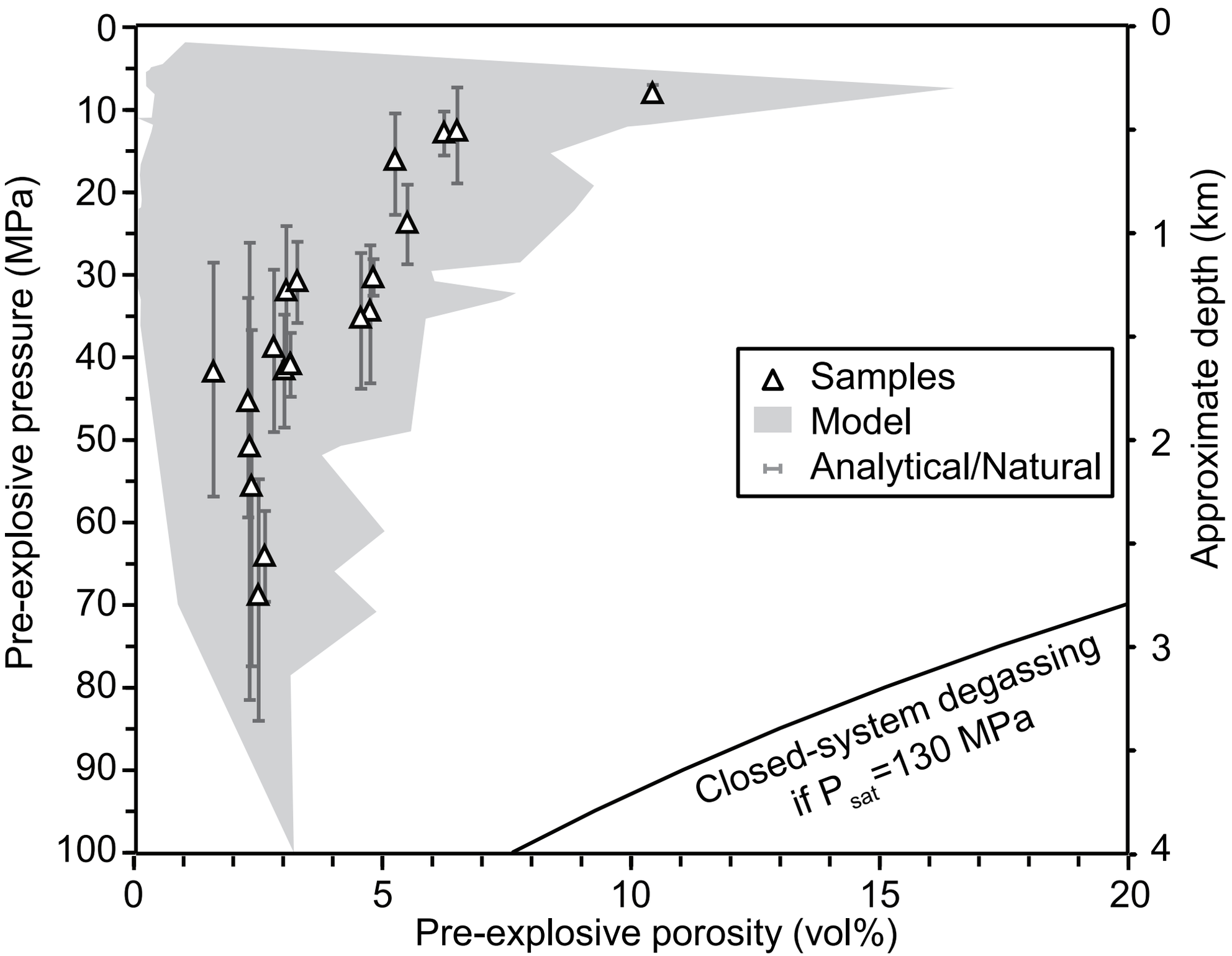
Pre-explosive pressure (MPa)
Approximate depth (km)
Pre-explosive porosity (vol%)
Samples
Model
Analytical/Natural
Closed-system degassing
if P sat=130 MPa
0
10
20
30
40
50
60
70
80
90
100
0
1
2
3
4
0
5
10
15
20

FIGURE 2

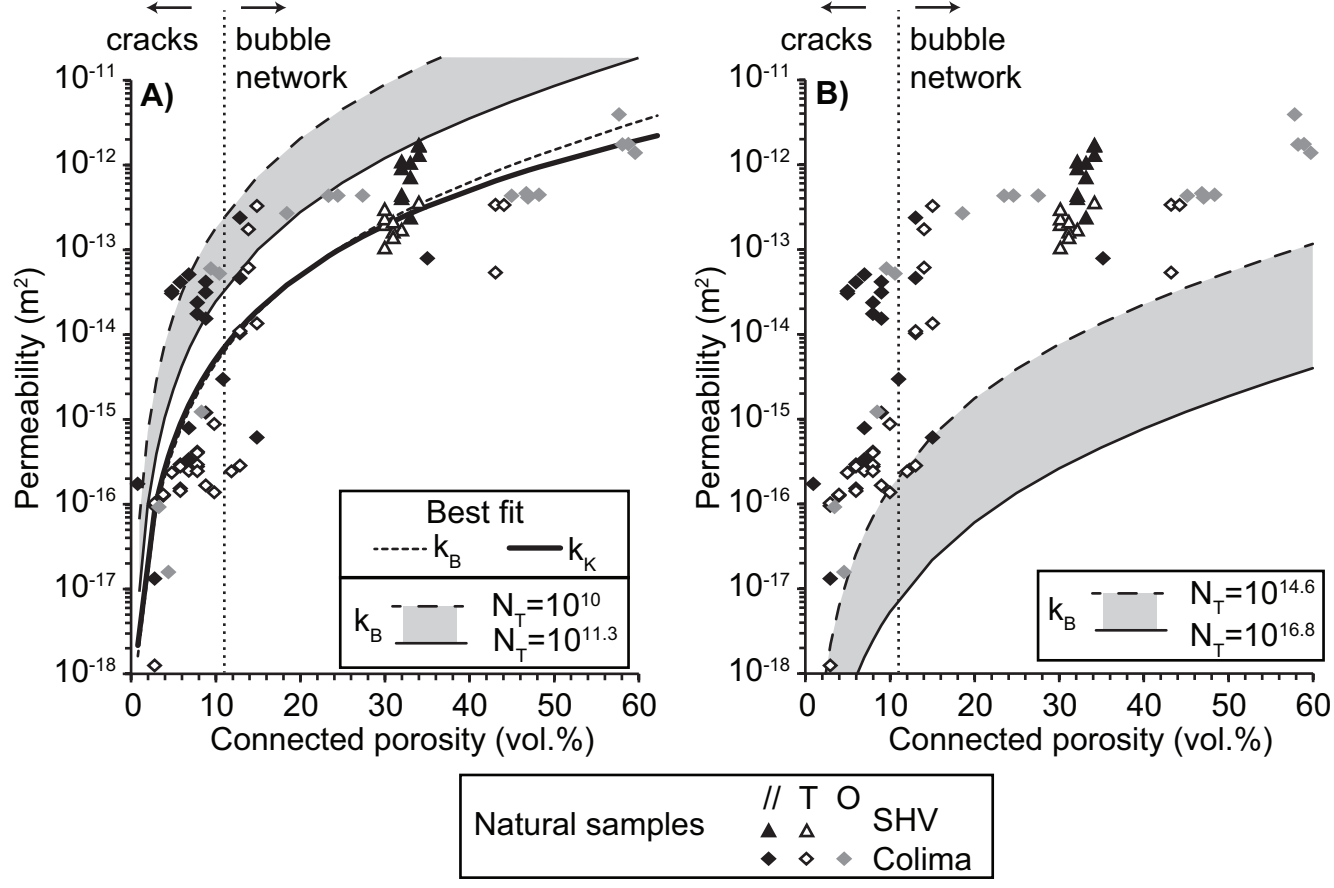
cracks
bubble network
A)
B)
Permeability (m²)
Connected porosity (vol.%)
Best fit
k_B
k_K
k_B
N_T=10^10
N_T=10^11.3
N_T=10^14.6
N_T=10^16.8
Natural samples
// T O
SHV
Colima

FIGURE 3

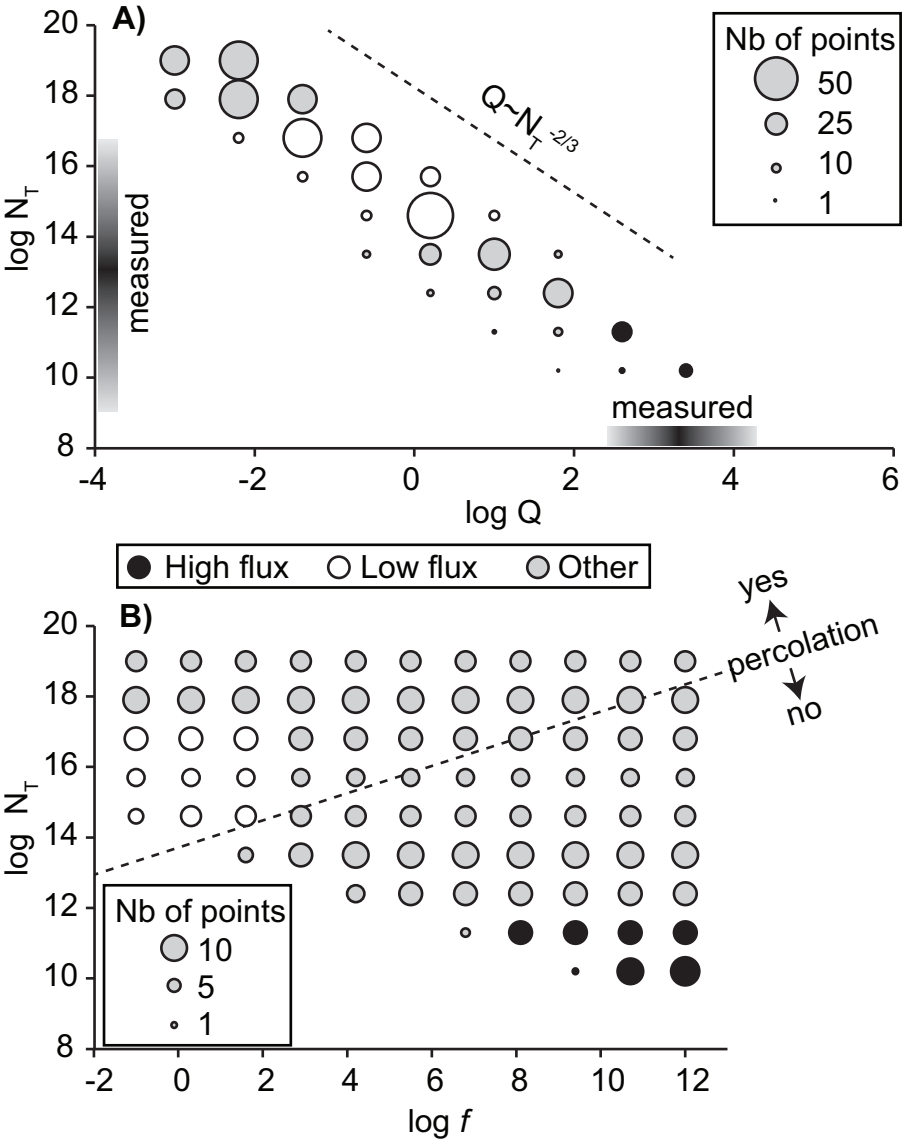
A)
Nb of points
50
25
10
1
Q~N_T^-2/3
measured
measured
log N_T
log Q
High flux
Low flux
Other
B)
yes
percolation
no
Nb of points
10
5
1
log N_T
log f

FIGURE 4

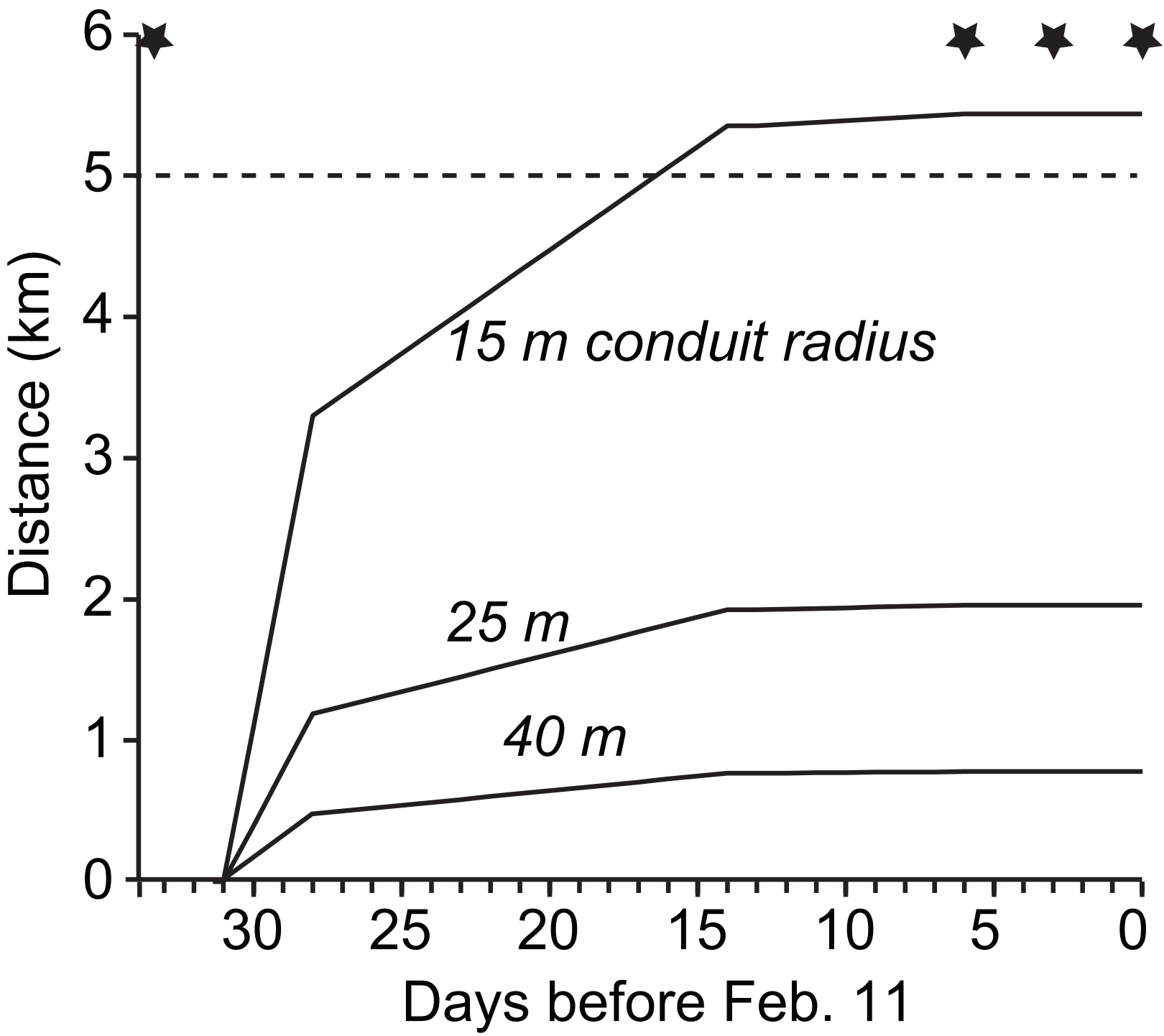
6
5
4
3
2
1
0
Distance (km)
15 m conduit radius
25 m
40 m
30
25
20
15
10
5
0
Days before Feb. 11

FIGURE 5

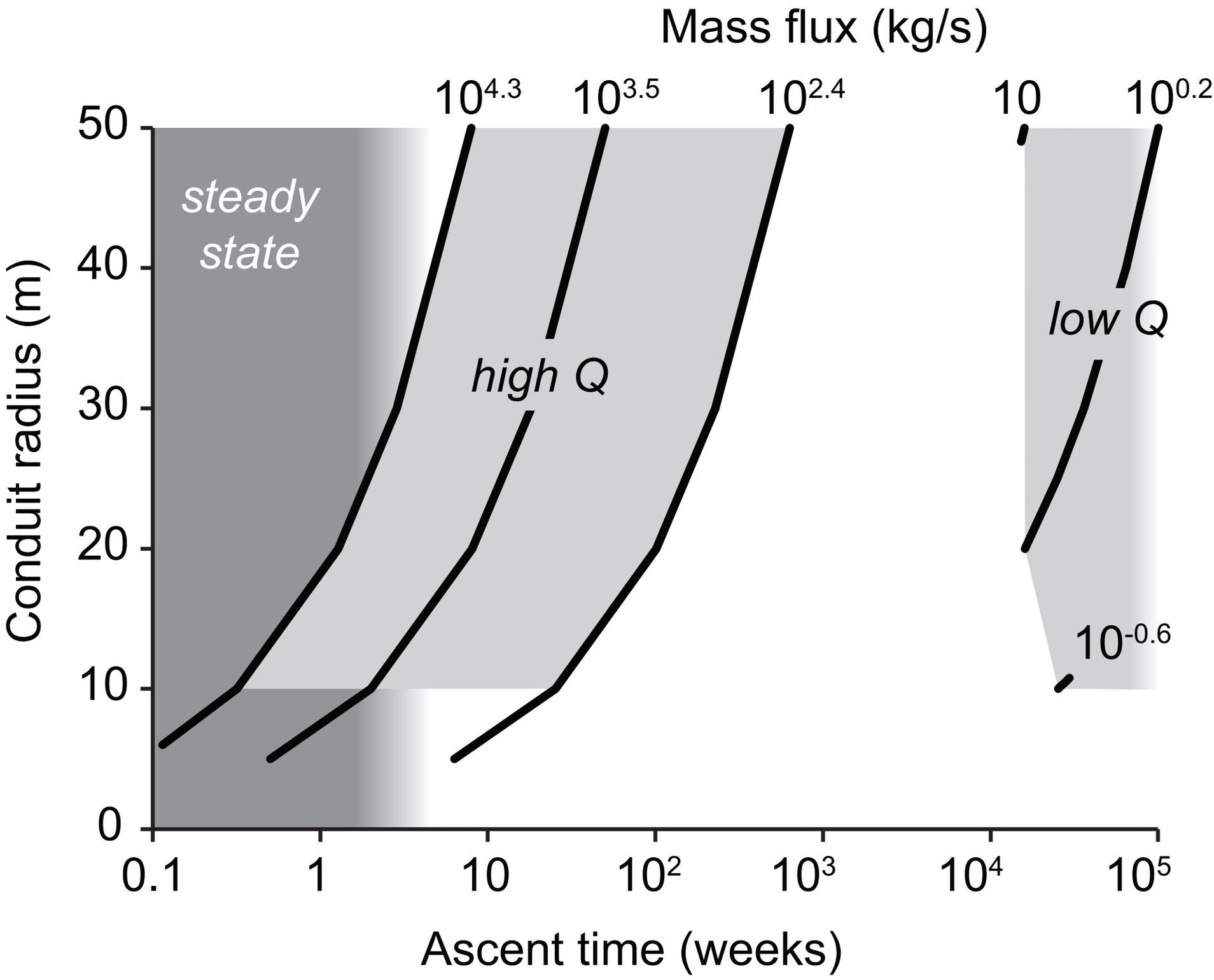
Mass flux (kg/s)
$10^{4.3}$
$10^{3.5}$
$10^{2.4}$
10
$10^{0.2}$
steady state
high Q
low Q
$10^{-0.6}$
Conduit radius (m)
50
40
30
20
10
0
0.1
1
10
10^2
10^3
10^4
10^5
Ascent time (weeks)

FIGURE 6

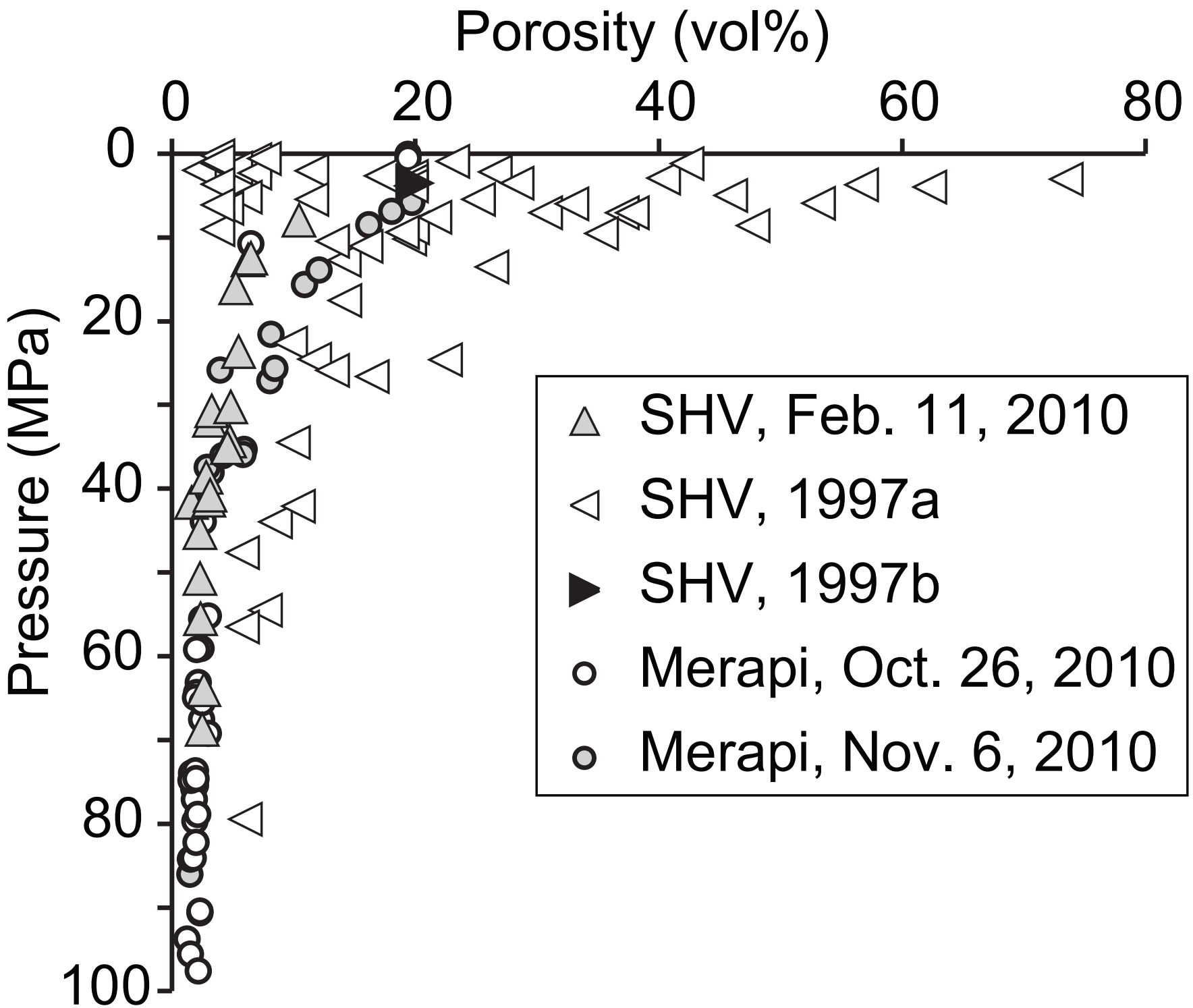
Porosity (vol%)
0
20
40
60
80
Pressure (MPa)
0
20
40
60
80
100
SHV, Feb. 11, 2010
SHV, 1997a
SHV, 1997b
Merapi, Oct. 26, 2010
Merapi, Nov. 6, 2010

FIGURE 7

Conduit processes during the February 11, 2010 Vulcanian eruption of Soufrière Hills, Montserrat

Alain BURGISSER[1*], Tonin BECHON[2], Laure CHEVALIER[1,3], Marielle COLLOMBET[1], Laurent ARBARET[4], Mélanie FORIEN[5]

[1] Univ. Grenoble Alpes, Univ. Savoie Mont Blanc, CNRS, IRD, IFSTTAR, ISTerre, 38000 Grenoble, France.

[2] Département de Géologie, Université de Liège, Allée du Six Août 12, 4000 Sart Tilman, Belgium.

[3] Now at: Institut für Geowissenschaften, Goethe Universität, Altenhöferallee 1, 60348 Frankfurt am Main, Germany.

[4] Institut des Sciences de la Terre d'Orléans (ISTO), Université d'Orléans-CNRS-BRGM, Orléans, France.

[5] Department of Geosciences, UiT The Arctic University of Norway in Tromsø, 9037 Tromsø, Norway.

* Corresponding author: Phone: (+33) 479 758 780. Fax: (+33) 479 758 742. Email: alain.burgisser@univ-savoie.fr

Supplementary Information

This Supplementary Information includes text providing additional details on the textural analysis and the conduit flow modeling (Text S1–S5), one table with GPS coordinates of the sampling locations (Table S1), and 6 figures (Figs. S1–S6).

Supplementary Text S1.

Weight fractions of water in the glass, X_{gl}, were calculated by neglecting the weight of the vesicles:

$$X_{gl} = \frac{X_{bulk}\sum_i V_i\rho_i - X_a C\, V_{a+cpx}\rho_a}{V_{gl}\rho_{gl}} \quad \text{(S1)}$$

where X_{bulk} is the bulk H_2O weight fraction, X_a = 0.02 is the H_2O weight fraction in amphibole, C = 0.95 is the assumed constant ratio between the volume fraction of amphibole and that of amphibole plus clinopyroxene (Murphy et al., 2000), V_i are volume fractions, and ρ_i are densities. The sum is $\sum_i V_i\rho_i = V_{opx}\rho_{opx} + V_{a+cpx}\rho_{a+cpx} + V_{gl}\rho_{gl} + V_{ox}\rho_{ox} + V_{qz}\rho_{qz} + V_{plg}\rho_{plg} + V_{oth}\rho_{oth}$ and the subscripts *opx*, *a+cpx*, *gl*, *ox*, *qz*, *plg*, *oth*, and *a* mean orthopyroxene, amphibole plus clinopyroxene, glass, oxide, quartz, plagioclase, other, and amphibole, respectively and where densities are $\rho_{opx} = \rho_{a+cpx} = \rho_a = \rho_{oth}$ =3300 kg/m^3, ρ_{gl} = 2380 kg/m^3, ρ_{ox} = 4720 kg/m^3, ρ_{qz} = 2650 kg/m^3, and ρ_{plag} = 2570 kg/m^3. Uncertainties on X_{gl} were calculated by error propagation (Drignon et al., 2016). The mineral separation procedure from Drignon et al. (2016) was adjusted to the phases present in our samples (Fig. 1B). Let F_j be the final binary images with the additional subscripts *ves* and *m+gl* being vesicles and matrix plus glass, respectively. Let I_k be the segmented elemental images per zoom level with k = Al, Si-m, Si-h, Fe-h, Fe-m, Mg, and Ca (X-m and X-h are medium and high threshold levels). The series of Boolean manipulations to obtain the final images reads:

$F_{ves} = I_{ves}$ OR NOT(I_{Al} OR I_{Ca} OR I_{Fe} OR I_{Mg} OR $I_{Si\text{-}h}$ OR $I_{Si\text{-}m}$ OR $I_{Fe\text{-}h}$ OR $I_{Fe\text{-}m}$)
$F_{ox} = I_{Fe\text{-}h}$
$J_i = I_i - F_{ves} - F_{ox}$
$F_{a+cpx} = J_{Ca}$ AND J_{Mg}
$K_i = J_i - F_{a+cpx}$
$F_{opx} = K_{Fe\text{-}m}$ AND K_{Mg}
$L_i = K_i - F_{opx}$
$F_{plg} = L_{Ca}$ AND L_{Al}
$M_i = L_i - F_{plg}$
$F_{qz} = M_{Si\text{-}h}$
$N_i = M_i - F_{qz}$
$F_{m+gl} = N_{Ca}$ OR $N_{Fe\text{-}m}$ OR N_{Mg} OR $N_{Si\text{-}m}$ OR $N_{Si\text{-}h}$ OR N_{Al}
$F_{oth} = 100\% - F_{ves} - F_{ox} - F_{a+cpx} - F_{opx} - F_{plg} - F_{qz} - F_{m+gl}$ (S2)

The sign minus implies image subtraction so that A-B corresponds to A AND NOT B in Boolean notation, and 100% corresponds to a full image area. Figure S2 illustrates the steps summarized by Eq. (S2)

Supplementary Text S2.

Figure S4 shows how bubble and oxide number densities were calculated by combining two image magnifications for sample AMO210A. This sample features a strong mismatch of size distribution between the two magnifications around 30 μm. The reconstruction procedure smooths this mismatch and creates a break in slope that translates into an apparent bimodality of the distribution across that length scale. The bubble-free number density reported in Table 2, however, is a cumulative sum of the distribution shown in Fig. S4. The cumulative sum is not sensitive to this artifact because it affects a number of bubbles much smaller (typically by 2–3 orders of magnitude) than that of the sum.

Supplementary Text S3.

Figure S5 shows bubble-free crystal content as a function of pre-explosive pressure. The natural variability far exceeds the trend calculated by a fit based on experimental data of crystal growth kinetics in the Soufriere Hills Volcano magma (Kozono and Koyaguchi, 2010), so we opted for a constant, average value of

crystal content.

Table S1: Sample locations in standard UTM zone 20N coordinates.

Location	Easting	Northing	Elevation (m)	Location
AMO210	589338	1852498	24	Farm River valley
WP1.095	588597	1851421	259	Harris Lookout
WP1.108	590487	1851591	33	Spanish Point
WP2.200	589696	1850761	116	White's Bottom Ghaut
WP2.201	590067	1850532	94	White's Bottom Ghaut
WP2.329b	588373	1851291	279	Harris Lookout

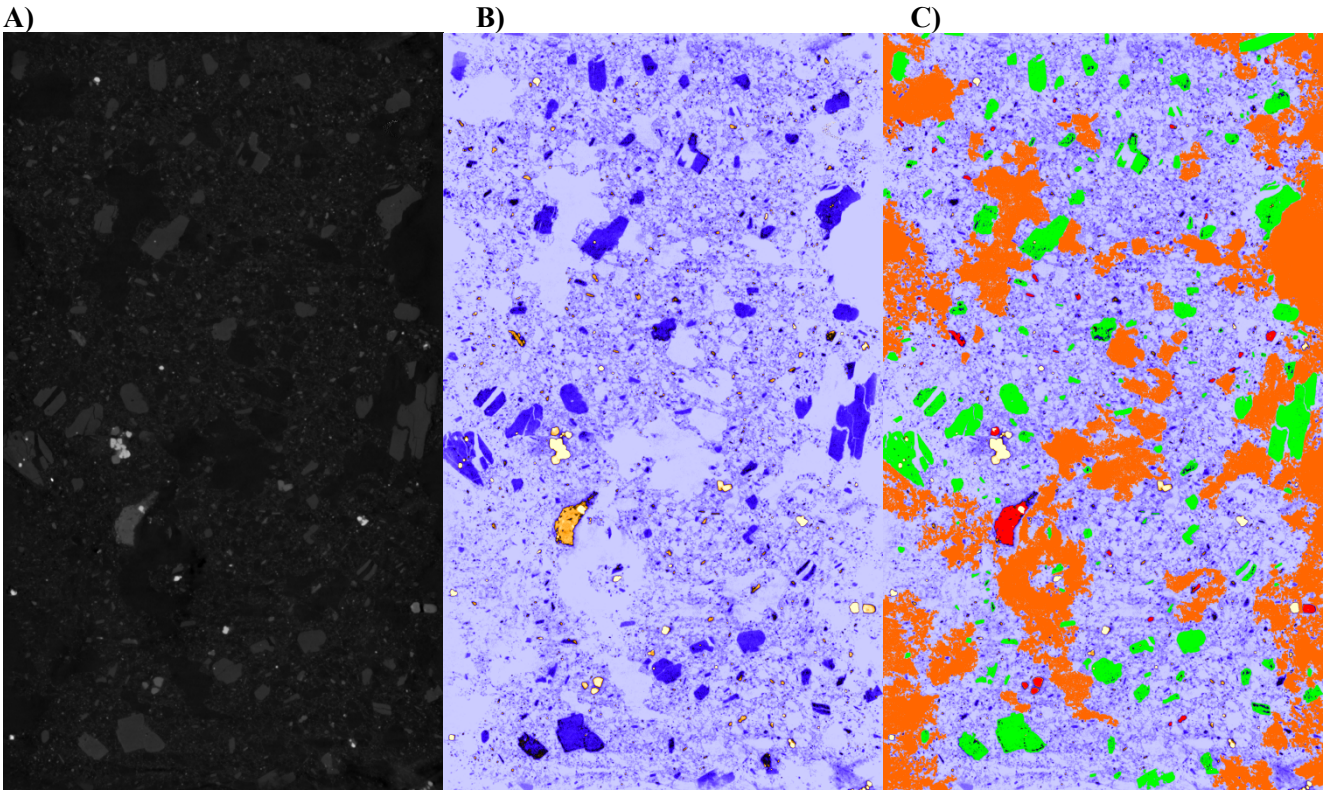

Figure S1: Representative tomographic slice of sample AMO210Q. Each image spans 1.34 cm horizontally. A) Grayscale image of X-ray attenuation levels. B) Same image as A) but with a color scheme highlighting the different mineral phases to aid automatic and manual segmentations. C) Segmented image. Analyzed objects are oxides (pale yellow), plagioclases (green), other minerals (red to dark yellow shades), matrix (dark shades of blue), vesicles with circularity <0.2 and equivalent size >300 μm (orange), and other vesicles (light blue).

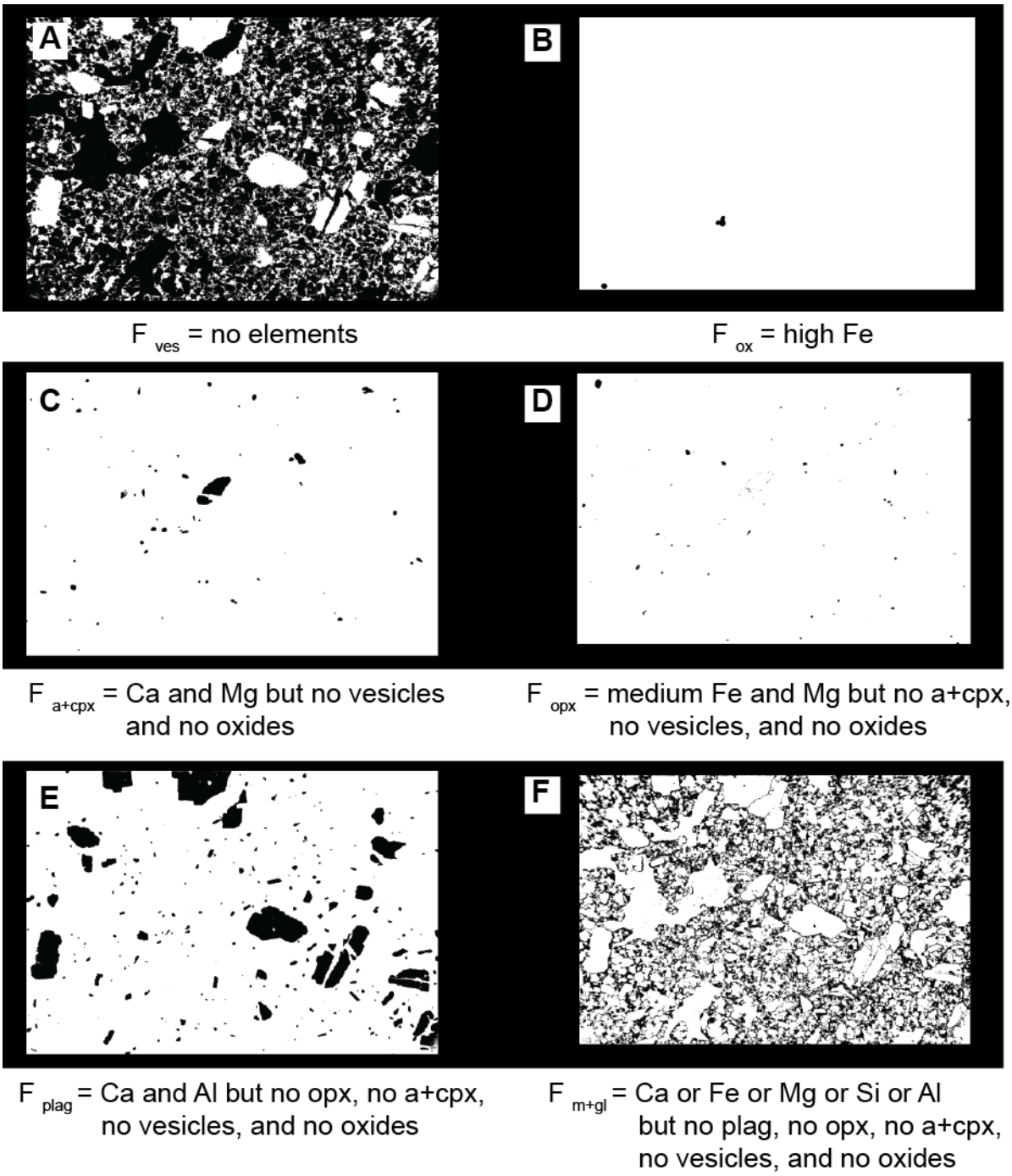

Figure S2: Mineral phase quantification by EDS for sample AMO210C (same image as that of Fig. 1). Images A)–F) correspond to the successive steps summarized in Eq. (S2) that result in the composite image on Fig. 1B.

A)

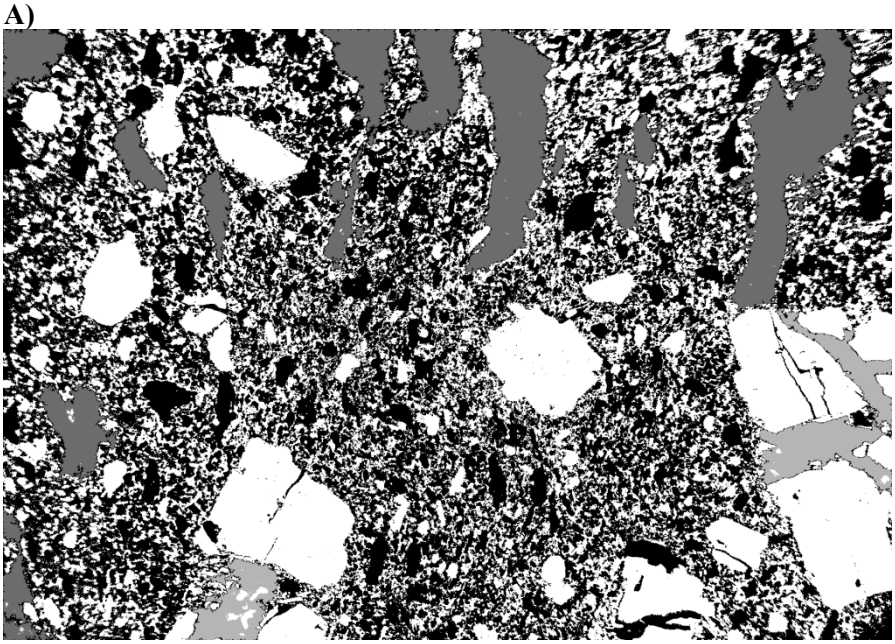

B)

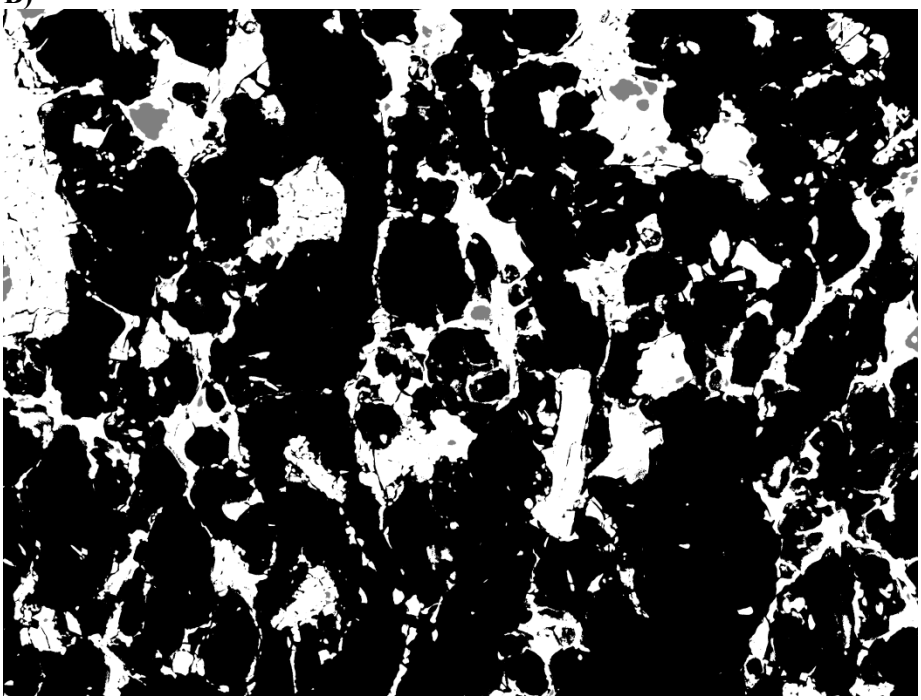

Figure S3: Representative pumice WP1.059B from the 2010 event. Minerals and glass are white. A) Composite grayscale ×50 image spanning 7 mm horizontally that contains parts of three of the four vesicle populations. Large vesicles >300 μm across and circularity <0.2 are divided into two populations. Population 1 (light grey) is composed of large, syn-explosive angular voids existing between crystal fragments that were segmented by hand. Population 2 (dark grey) is composed of the remaining large vesicles, which are classified as pre-explosive. The coarse part of population 3 (black) is composed of all the vesicles that do not belong to the first two populations. B) Composite grayscale ×1000 image spanning 436 μm horizontally that contains parts of populations 3 and 4. Black vesicles compose the fine part of population 3. Population 4 (grey) is composed of rounded, syn-eruptive vesicles <50 μm across and circularity >0.4.

A) B)

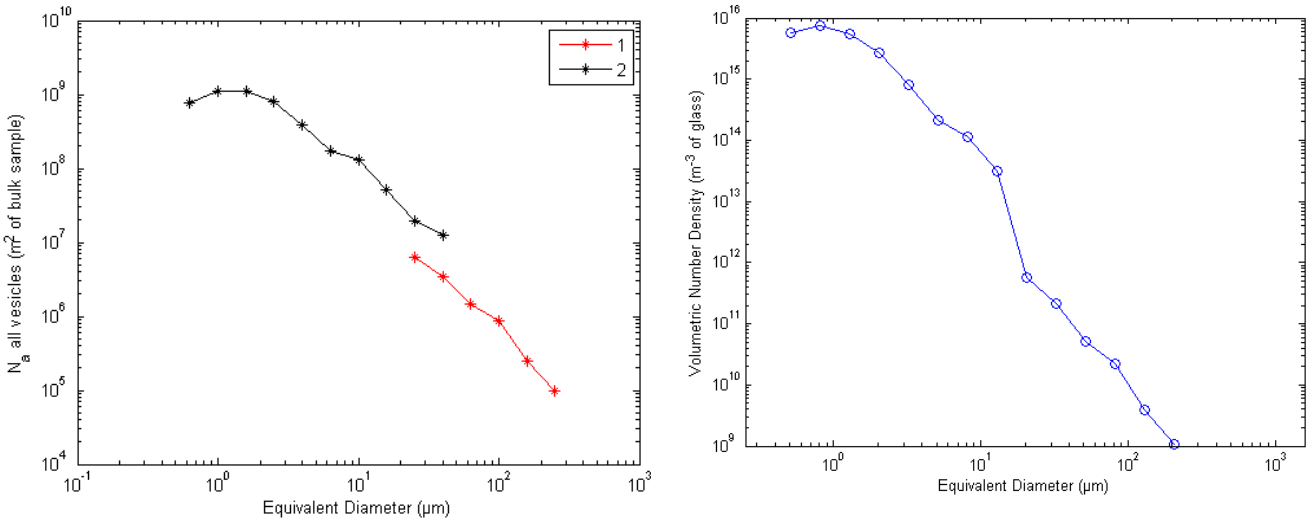

Figure S4: Bubble size distribution reconstruction of sample AMO210A following the method by Giachetti et al. (2010). A) Number of all vesicles per m^2 of glass for each magnification used (1: ×2000 and 2: ×50). B) Combination of the 2 magnifications with a cut-off of 30 µm followed by 3D conversion obtained using 2D data and stereological transformations from Cheng and Lemlich (1983). The number density reported in Table 2 for AMO210A is the cumulative sum of the distribution in B).

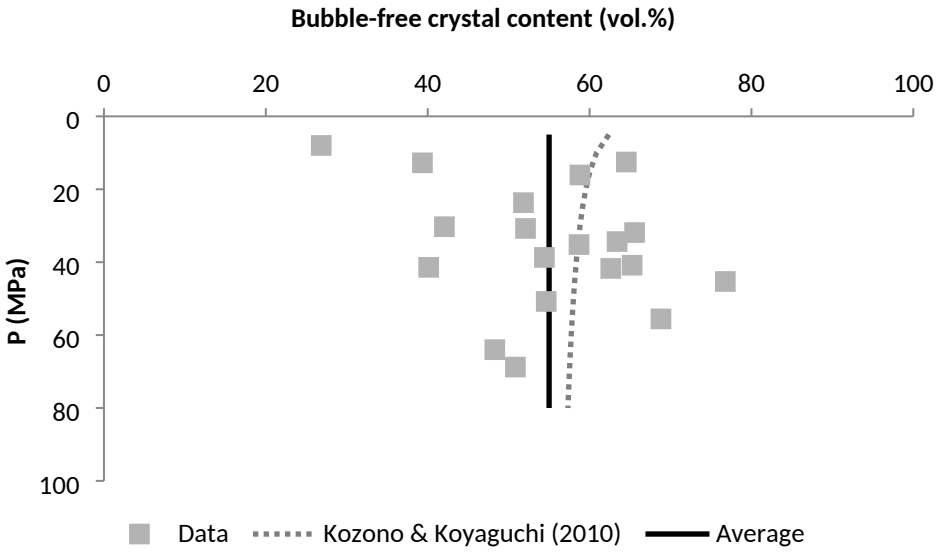

Figure S5: Sample crystal contents (squares) as a function of pre-explosive pressure (*P*). The vertical line indicates the average value of 55 vol.% that we chose in our simulations. The dotted line corresponds to the fit based on experimental data of crystal growth kinetics for the Soufriere Hills Volcano magma used by Kozono and Koyaguchi (2010).

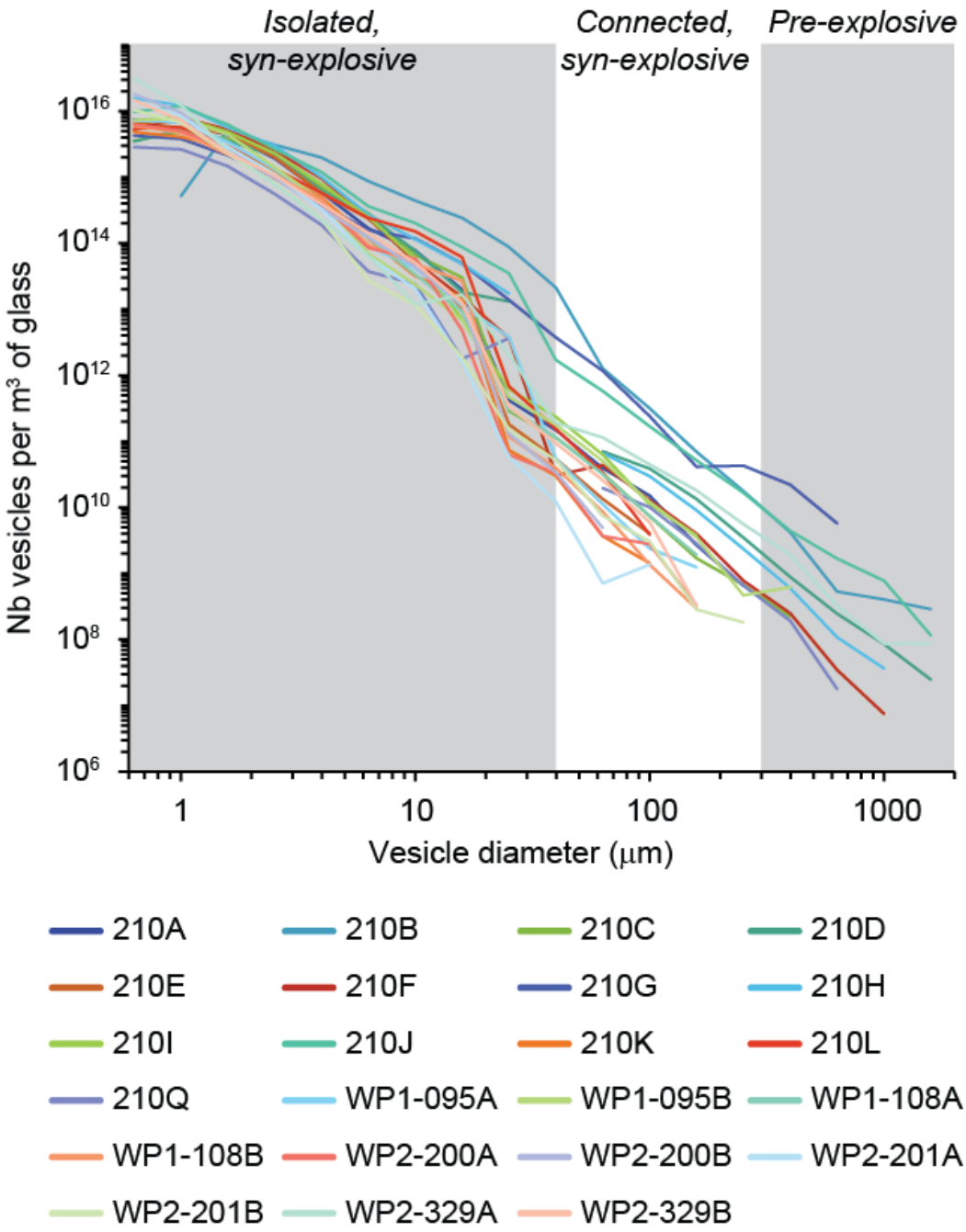

Figure S6: Bubble size distributions of samples listed in Table 2. Vertical boundaries roughly correspond to vesicle origin (pre- or syn-explosive). These boundaries are only indicative because the origin discrimination is made on the joint basis of size and circularity.